



# **NUMERICAL MODELING OF FLOW IN A MIST ELIMINATOR FOR GEOTHERMAL POWER PLANTS**

Matti Arnim Grabo



**Faculty of Industrial Engineering,  
Mechanical Engineering and Computer Science  
University of Iceland  
2016**



# **NUMERICAL MODELING OF FLOW IN A MIST ELIMINATOR FOR GEOTHERMAL POWER PLANTS**

Matti Arnim Grabo

30 ECTS thesis submitted in partial fulfillment of a  
*Magister Scientiarum* degree in Innovative and Sustainable  
Energy Engineering

Advisors  
Halldór Pálsson  
Vigfús Arnar Jósefsson

Faculty Representative  
Ármann Gylfason

Faculty of Industrial Engineering, Mechanical Engineering and  
Computer Science

School of Engineering and Natural Sciences

University of Iceland  
Reykjavik, June 2016

NUMERICAL MODELING OF FLOW IN A MIST ELIMINATOR FOR  
GEOTHERMAL POWER PLANTS

30 ECTS thesis submitted in partial fulfillment of a *Magister Scientiarum* degree in Innovative and Sustainable Energy Engineering

Copyright © 2016 Matti Arnim Grabo  
All rights reserved

Faculty of Industrial Engineering, Mechanical Engineering and Computer Science  
School of Engineering and Natural Sciences  
University of Iceland  
Hjarðarhagi 2-6  
107, Reykjavík  
Iceland  
Telephone: 525 4700

Bibliographic information:

Matti Arnim Grabo, 2016, *Numerical modeling of flow in a mist eliminator for geothermal power plants*, Master's thesis, Industrial Engineering, Mechanical Engineering and Computer Science, University of Iceland

Printing: Háskólaprent ehf., Fálkagata 2, 107 Reykjavík  
Reykjavík, Iceland, June 2016

---

# Abstract

Considering both durability and electricity production, the quality of steam extracted from a geothermal well and led into the turbine has an important impact on the overall performance of a geothermal power plant. To increase the steam quality, i.e. the share of pure steam in the two-phase mixture, horizontal mist eliminators are commonly used in industry. These devices consist of a drum in which the fluid is expanded and guided through a filter, where the droplets are separated from the steam.

The design process of mist eliminators is often based on empirical data and the flow inside the drum is not well understood, yet. Hence, numerical simulations with the freeware OpenFOAM were performed during this project to develop a wider understanding of the single-phase flow behavior inside the eliminator.

Eleven simulations were performed including three simulations as part of a mesh sensitivity analysis, one to investigate different numerical schemes and two simulations with different turbulence models. Further, three cases were run with varying inlet velocities and two with different inlet/outlet configurations.

First, an appropriate simulation setup could be found based on comparison with a reference value and recommendations from the literature. This setup included a medium sized mesh (50 mm cell size), upwind scheme discretization and the  $k-\omega$ -SST turbulence model. Second, the variation of the inlet velocities could be used to manipulate the pressure drop and the flow distribution within the wire mesh. Third, both of the geometry changes gave higher overall pressure losses however, the flow distribution inside the wire mesh could be improved by the usage of vertically attached inlet pipes.



---

*To my parents Arnim and Dagmar*





---

# Contents

<b>List of Figures .....</b>	<b>ix</b>
<b>List of Tables.....</b>	<b>xiii</b>
<b>Nomenclature.....</b>	<b>xv</b>
Abbreviations.....	xv
Latin symbols.....	xv
Greek symbols .....	xvii
Indices.....	xvii
<b>Acknowledgements .....</b>	<b>xix</b>
<b>1 Introduction.....</b>	<b>1</b>
<b>2 Mist eliminators in geothermal applications.....</b>	<b>3</b>
2.1 General information on geothermal power plants.....	3
2.2 Mist eliminator designs .....	4
2.2.1 Cyclone mist eliminators .....	4
2.2.2 Horizontal mist eliminators.....	5
<b>3 Theory.....</b>	<b>7</b>
3.1 Governing equations.....	7
3.2 Turbulence modeling.....	8
3.2.1 REYNOLDS-averaged momentum and continuity equations.....	9
3.2.2 The $k$ - $\varepsilon$ model.....	10
3.2.3 The $k$ - $\omega$ -SST model .....	12
3.2.4 The SPALART-ALLMARAS model .....	14
3.3 Discretization.....	14
3.3.1 Spatial discretization.....	15
3.3.2 Discretization of the governing equations .....	15
3.3.3 Temporal discretization .....	17
3.4 Treatment of a porous wire mesh.....	17
<b>4 Case study.....</b>	<b>19</b>
4.1 Modeling of the current mist eliminator design .....	19
4.1.1 Geometry creation.....	19
4.1.2 Meshing.....	21
4.1.3 Boundary conditions .....	22
4.1.4 Discretization schemes.....	24

4.2	Simulation variants .....	25
4.2.1	Influence of the simulation setup.....	26
4.2.2	Change of boundary conditions.....	28
4.2.3	Change of the geometry.....	28
4.3	Evaluation criteria .....	30
4.3.1	Quantitative criteria .....	31
4.3.2	Qualitative/visual criteria .....	32
4.3.3	Computational criteria .....	32
<b>5</b>	<b>Results.....</b>	<b>33</b>
5.1	Initial case .....	33
5.2	Influence of the simulation setup .....	37
5.2.1	Mesh sensitivity .....	37
5.2.2	Influence of the chosen numerical schemes .....	38
5.2.3	Influence of the chosen turbulence models .....	40
5.3	Change of boundary conditions .....	42
5.4	Geometry changes.....	47
5.5	Summary .....	52
<b>6</b>	<b>Conclusion and outlook.....</b>	<b>55</b>
	<b>References .....</b>	<b>57</b>
	<b>Appendix A: Estimation of the wall distance.....</b>	<b>59</b>
	<b>Appendix B: Calculation of the turbulent boundary conditions .....</b>	<b>60</b>
	<b>Appendix C: Calculation of the FORCHHEIMER coefficients .....</b>	<b>61</b>
	<b>Appendix D: Overview of simulation results.....</b>	<b>62</b>

---

## List of Figures

Figure 2.1: Schematic of a single-flash geothermal power plant .....	4
Figure 2.2: Vertical cyclone separator [4] .....	5
Figure 2.3: Typical horizontal mist eliminator configurations [5], with friendly permission from AMACS .....	6
Figure 3.1: Two neighboring finite volumes (cells) [11] .....	15
Figure 4.1: 3D-model of the internal volume of the mist eliminator .....	20
Figure 4.2: Overview of patches used for modeling and post-processing .....	21
Figure 4.3: Solid eliminator geometry (left) and a mesh cross section (right) .....	22
Figure 4.4: Velocity profile in one inlet pipe with (left) and without mapping (right) .....	24
Figure 4.5: Mesh xy-cross-section of the case originalCoarse .....	26
Figure 4.6: Mesh xy-cross-section of the case originalMedium .....	27
Figure 4.7: Mesh xy-cross-section of the case originalRefined .....	27
Figure 4.8: Eliminator design case topInletOutlet .....	29
Figure 4.9: Eliminator design case topOutletMerged .....	29
Figure 4.10: The four patches used for data sampling .....	31
Figure 5.1: Velocity distribution inside the mist eliminator for the initial case showing jet streams and separation in the outlet header .....	33
Figure 5.2: Pressure contour plot over the xy-plane inside the mist eliminator for the initial case showing the main pressure losses after the right outlet pipe .....	34
Figure 5.3: Turbulent intensity at the outlet pipes for the initial case showing turbulence in the mid and right outlet pipes and the gathering pipe .....	34
Figure 5.4: Velocity components in y-direction filter inlet porousIn to filter outlet porousOut for the initial case showing the suction zones below the outlet pipes .....	35

Figure 5.5: Velocity magnitude stream lines for the initial case showing that the main share of flow is sucked through the right outlet pipe .....	36
Figure 5.6: Pressure drop over the filter as function of the cell size.....	38
Figure 5.7: Comparison of the velocity distribution over the filter middle plane porousMid for the cases originalMedium and originalUpwind .....	39
Figure 5.8: Velocity contour plot for the case originalSST showing the right upper corner of the xy-plane with gathering pipe and separation zones after the outlet pipes .....	41
Figure 5.9: Velocity contour plot for the case originalMedium showing the right upper corner of the xy-plane with gathering pipe and separation zones after the outlet pipes .....	41
Figure 5.10: Velocity contour plot for the case originalSpAllm showing the right upper corner of the xy-plane with gathering pipe and separation zones after the outlet pipes .....	42
Figure 5.11: Pressure drop over filter for different mass flow distributions at the inlets .....	43
Figure 5.12: Pressure plot over the xy-plane inside the drum for the case originalVarU7525 showing the pressure difference between the left and right part of the drum.....	44
Figure 5.13: Mass flow ranges of the vertical outlet pipes for varying inlet velocities, e.g. for originalVarU4060 27% of the flow streamed through the left pipe and 41.3% through the right one, thus the mass flow range was 14.3%.....	44
Figure 5.14: Velocity distribution over the filter middle plane porousMid for different inlet mass flows showing how the main suction zone moves further to the right with higher velocity at the left inlet .....	45
Figure 5.15: Velocity cross section over the xy-plane of the eliminator for different inlet velocities showing their impact on the development of the jet streams.....	46
Figure 5.16: Velocity contour plot over the xy-plane for the case topInletOutlet after two different periods of time showing the time dependency of the jet streams' shape .....	48
Figure 5.17: Velocity plot over the filter middle plane porousMid for different inlet and outlet configurations .....	49

---

Figure 5.18: Turbulent intensity plot over the xy-plane for the case <code>outletMerged</code> and <code>topInletOutlet</code> showing a much more tranquilized regime for the latter case .....	50
Figure 5.19: Velocity contour plot over the xy-plane for the case <code>topOutletMerged</code> .....	51
Figure 5.20: Pressure profile in the T-connection for the case <code>topOutletMerged</code> showing high pressure losses in the horizontal gathering pipe.....	51



---

## List of Tables

Table 3.1: Closure constants for the $k$ - $\omega$ -SST model [9].....	13
Table 4.1: Name convention and functionality of patches and faces used for the mist eliminator models .....	21
Table 4.2: Velocity BCs for the initial simulation setup .....	23
Table 4.3: Pressure BCs for the initial simulation setup .....	23
Table 4.4: Mesh properties for the mesh sensitivity analysis.....	26
Table 4.5: Overview of all simulation variants .....	30
Table 5.1: Results for the initial case after 10 s; values for the three outlet pipes from left to right are separated by a backslash (row 7 and 9) .....	36
Table 5.2: Results for different mesh sizes.....	37
Table 5.3: Comparison of results between the initial case and the case run with upwind schemes.....	39
Table 5.4: Results for three different turbulence models for the initial design.....	40
Table 5.5: Results of the inlet velocity variation for the initial design .....	43
Table 5.6: Results for different outlet and inlet configurations.....	47
Table 5.7: Summary of results obtained from varied inlet velocities.....	53
Table 5.8: Summary of results obtained from varied inlet/outlet configurations.....	53





---

# Nomenclature

## Abbreviations

CAD	Computer Aided Design
CDS	Central Differencing Scheme
CFD	Computational Fluid Dynamics
BC	Boundary Condition
FVM	Finite Volume Method
LES	Large Eddy Simulation
OpenFOAM	Open Field Operation And Manipulation
SST	Shear Stress Transport
UD	Upwind Differencing
vel.	Velocity

## Latin symbols

$a$	-	coefficient in turbulence modeling
$C$	-	coefficient in turbulence modeling
$c$	-	coefficient in the SPALART-ALLMARAS turbulence model
$CD$	-	factor for $k$ - $\omega$ -SST blending function
$CFL$	-	COURANT number
$d$	$m, \frac{1}{m}$	distance from wall, DARCY coefficient
$F$	$N, -$	generic body force, factor for $k$ - $\omega$ -SST blending function

$f$	-	coefficient in the SPALART-ALLMARAS model, FORCHHEIMER coefficient
$k$	$\frac{m^2}{s^2}$	turbulent kinetic energy
$L$	$m$	characteristic length
$l$	$m$	length, turbulent length scale
$I$	-	turbulent intensity
$p$	$Pa$	pressure
$Q$	$\frac{m^3}{s}$	volumetric flow
$Re$	-	REYNOLDS number
$S$	$s^{-1}$	strain rate invariant
$t$	$s$	time
$U$	$\frac{m}{s}$	velocity
$V$	$m^3$	control volume
$w$	$m$	width
$x$	$m$	direction, distance
$y$	$m$	wall distance

---

## Greek symbols

$\beta$	-	coefficient in turbulence modeling
$\gamma$	-	factor for $k$ - $\omega$ -SST blending function
$\varepsilon$	$\frac{m^2}{s^3}$	dissipation rate
$\vartheta$	-	porosity
$\lambda$	-	distance ratio
$\mu$	$\frac{kg}{m \cdot s}$	dynamic viscosity
$\nu$	$\frac{m^2}{s}$	kinematic viscosity, eddy viscosity
$\rho$	$\frac{kg}{m^3}$	density
$\sigma$	-	coefficient in turbulence modeling
$\tau$	$\frac{N^2}{m}$	stress tensor
$\phi$	-	generic flow field quantity
$\psi$	-	blending factor
$\omega$	$s^{-1}$	turbulent kinetic frequency

## Indices

$d$	droplet
$f$	face, filter
$g$	gaseous
$i$	spatial direction
$in$	inlet

## Nomenclature

---

$j$	repeated index for EINSTEIN summation
$k$	turbulent kinetic energy
$N$	neighbor cell
$n$	new value (current time step)
$o$	old value (previous time step)
$out$	outlet
$P$	present cell
$T$	turbulent, total
$V$	volume of pores

---

# Acknowledgements

This master thesis was written under the supervision of Associate Professor Halldór Pálsson, Faculty of Industrial Engineering, Mechanical Engineering and Computer Science, University of Iceland and M.Sc. Vigfús Arnar Jósefsson, Verkís Consulting Engineers. I sincerely want to thank them for their help and guidance throughout all stages of the work.

Further, my honest gratitude goes to Landsvirkjun for their financial aid in form of a scholarship. This monetary support helped to stay focused, particularly in the late stages of the project.

This work marks the final step of the master program Innovative and Sustainable Energy Engineering (ISEE) and I want to thank the organizers, especially Gabriella Tranell and Ida Johanne Ulseth at NTNU, for the development of the program. It was and still is a great experience and I am convinced that it will be beneficial for my future work life.

Also, my thank goes to Chalmers Technical University and the program coordinator in charge, David Pallarès, for my first year of the ISEE program in Gothenburg, Sweden. The study effort was high but valuable and I would not want to miss the long nights spent in the computer labs with my fellow classmates and friends Pálmar, Eric, Maria, Höfi, Carlo and Harpa. I hope our paths will cross again during our future careers.

For her patience and appreciation during the writing process and for the correction of my written English I want to thank my lovely girlfriend Kirby. Your support kept me motivated and our daily coffee meetings made me start the day with joy.

My last and deepest gratitude goes to my parents Arnim and Dagmar, who, with their emotional and financial support, made it possible to successfully begin and complete these studies. I hope to pay back all the things you have done for me eventually.



---

# 1 Introduction

The utilization of geothermal energy contributes to a sustainable way of thermal and electrical energy production. The lifetime of the equipment and particularly of the steam turbine is a major factor for the feasibility of a geothermal power plant. The quality of steam extracted from a geothermal well and led into the turbine has an important impact on the power plant's performance when both durability and electricity production are considered. Thus, the steam quality is one of the most influential parameters to be controlled during operation.

In a geothermal power plant, the extracted geothermal fluid is separated into steam and liquid in one or more separator stages in order to reach a steam content of at least 98% in the fluid. This means that 2% of the mixture is still liquid in the form of small droplets, which can be harmful to the turbine blades. Thus, to avoid damages, a *horizontal mist eliminator* can be used to increase the steam quality up to 99.99%. This device consists of a drum in which the fluid is expanded and guided through a filter, where the droplets are separated from the steam. The mist eliminator is located close to the turbine, whereas the separator can be located close to the wells or on the plant site depending on the steam gathering system in use [1].

The designs of both separators and mist eliminators are currently a result of experience and more or less created according to rules of thumb. To improve the performance and investigate possible material savings, numerical simulations were performed during this project in order to obtain a better understanding of the flow field inside the drum. Since the droplets were expected to be very small by volume and weight the simulations were set up as single-phase problem, i.e. it was assumed that the droplets follow the main flow field and do not interact with the gaseous phase. This assumption could be made for mist eliminators, but not for separators where the liquid content is much higher.

Several investigations using numerical methods have been made on separators for horizontal and vertical designs using the multiphase approach (see [2] and [3]). Investigations on the single-phase flow behavior inside a mist eliminator, however, have not been performed to current date according to the author's literature review. Since in this work the scope lies on horizontal mist eliminators and the physical phenomena utilized for the separation process are different, the vertical cyclone design is only discussed very briefly.

The program used to model the cases and to perform the simulations was the freely available C++-toolbox *OpenFOAM* (Open Field Operation And Manipulation) managed and distributed by OpenCFD<sup>®</sup>. It allows the development of numerical solvers used for solving problems of continuum physics as, for example, in *computational fluid dynamics* (CFD). It was developed at *Imperial College, London*, by HENRY WELLER in the late 1980s and is

still updated according to new research and experiences. Numerous models have been implemented since then, including models for turbulence, multiphase flow, heat transfer, chemical reactions as well as different solvers and discretization schemes. Only a few of these models were used during this case study, however.

To summarize, the aim of this project was to give a better understanding of the single-phase flow behavior inside horizontal mist eliminators. Furthermore, the setup of the simulations regarding factors such as turbulence models and mesh sensitivity as well as boundary conditions was investigated. Finally, the results could be used as reference in future design processes.



---

## **2 Mist eliminators in geothermal applications**

A geothermal power plant generates electricity and/or heat from steam extracted from an underground geothermal reservoir. Thereby, the properties of steam vary depending on the thermodynamic and chemical composition of the geothermal brine. One of the most crucial parameters is the steam quality, determining – among other parameters – the possible power output and the lifetime of the turbine. Usually the steam quality should be kept as high as possible before the flow enters the turbine to increase the productivity and to avoid damages by water droplets impinging the turbine blades. This can be realized by including a mist eliminator between the separator and the turbine inlet, which can increase the steam quality up to 99.99% by weight. Two different types of eliminators are commonly used, namely the horizontal type and the vertical cyclone type.

The following chapter gives a short overview on the basic structure of geothermal power plants, different types of mist eliminators and their functionality.

### **2.1 General information on geothermal power plants**

The general structure of a typical geothermal power plant is based on the RANKINE cycle and shown in Figure 2.1.

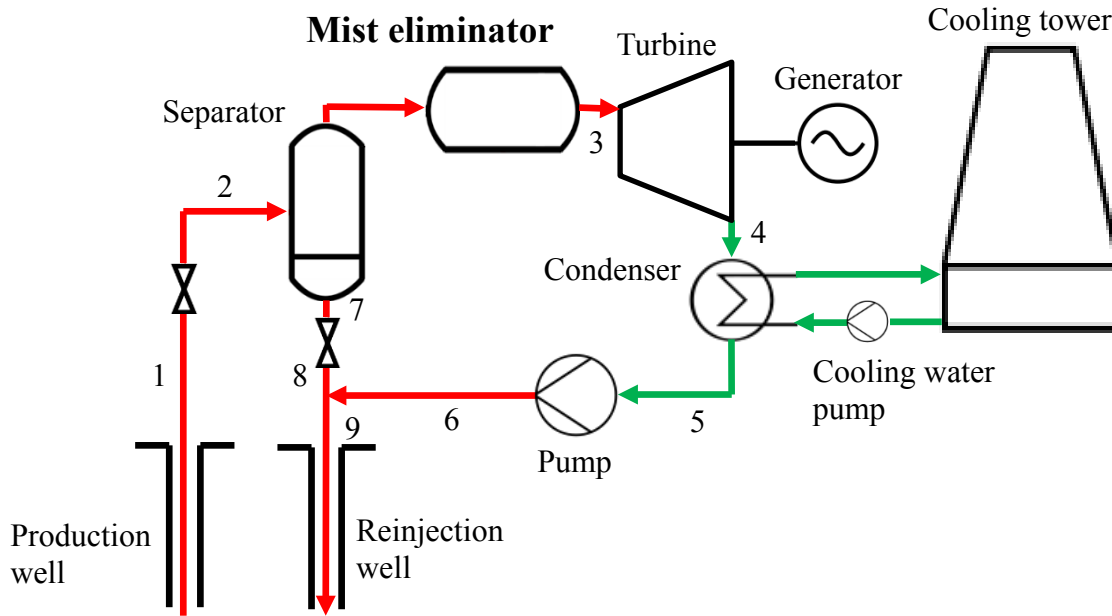


Figure 2.1: Schematic of a single-flash geothermal power plant

The brine is extracted from the production well (point 1) and then flashed by an expansion valve (points 1 to 2), i.e. part of the brine evaporates due to a pressure decrease. Since only steam can be utilized to generate electricity in the turbine it needs to be separated from the remaining brine through a separation process, which takes place in one or more separators and mist eliminators (points 2 to 3). In the turbine, the steam is expanded generating electricity through a generator driven by the shaft of the turbine (points 3 to 4). After the steam leaves the turbine it is condensed into liquid in a condenser (point 4 to 5) and pumped back into the reservoir through a reinjection well (points 6/7 to 9).

As mentioned before, the mist removal is part of the separation process and is usually located very close to the turbine, whereas the separator can be located further upstream.

## 2.2 Mist eliminator designs

### 2.2.1 Cyclone mist eliminators

The cyclone eliminator uses centrifugal forces to separate water from the steam. The two phase flow enters the cyclone with relatively high velocities up to 60 m/s and is forced into a helical pattern by the cyclonic shape. The heavier droplets gather at the walls and form a layer of water flowing down to a tank due to gravity. The steam exits the separator through a pipe at the top. The flow rate and the geometry determine the so called *cut point*, which is the size of the droplets removed from the stream with an efficiency of at least 50% [4].

Figure 2.2 shows the separation process in a vertical steam separator.

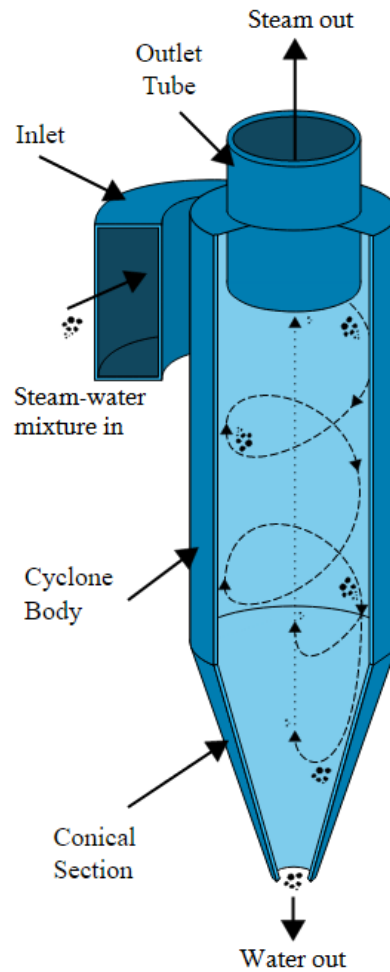


Figure 2.2: Vertical cyclone separator [4]

This eliminator type is a proven design and has shown high reliability in the past. Also, if the design is sophisticated no internal equipment as filters or wire meshes, is needed to improve the separation process. However, its operation range is quite small and lies only within  $\pm 10\%$ , since the geometry determines the cut point, i.e. if the inlet velocity varies too much the separation efficiency decreases rather quickly. Furthermore, the visual impact is big since the drum could reach heights up to several meters. This also makes the construction susceptible to high wind and seismic loads, which have to be accounted for by strong supports, increasing material cost [1].

### 2.2.2 Horizontal mist eliminators

The horizontal gravity separator has been used since the 1990s for geothermal applications and is therefore a rather new component in geothermal power plants. In mist eliminators of this design type, the steam flows into a big drum in which it is expanded and slowed down. Next, it is guided through a wire mesh or filter, fine enough so that the water droplets attach to the wires. After the droplets reach a certain mass, they fall down due to gravity and flow into a separate tank. When the steam leaves the mesh, it should have a quality of at least 99.9% by weight.

The biggest advantage of horizontal mist eliminators is the flexibility of their design, since the separation efficiency is not as dependent on the geometry as for the cyclone type. Thus, the operation range lies between 50 and 110% [1]. Furthermore, the visual impact is much lower compared to the cyclone type and the drum is less exposed to wind loads. Also, maintenance and installation are easier. However, an internal mesh is needed, which imposes an additional pressure drop and needs to be cleaned regularly.

Figure 2.3 shows two possible configurations for horizontal mist eliminators. The location and orientation of the mesh can either be vertical or horizontal. Further, the inlet pipes can be vertically attached to the drum as in the cases below, or from the side caps. Also, the number of inlets and outlets can be chosen rather arbitrarily. This leaves a lot more room for design optimization compared to the vertical type.

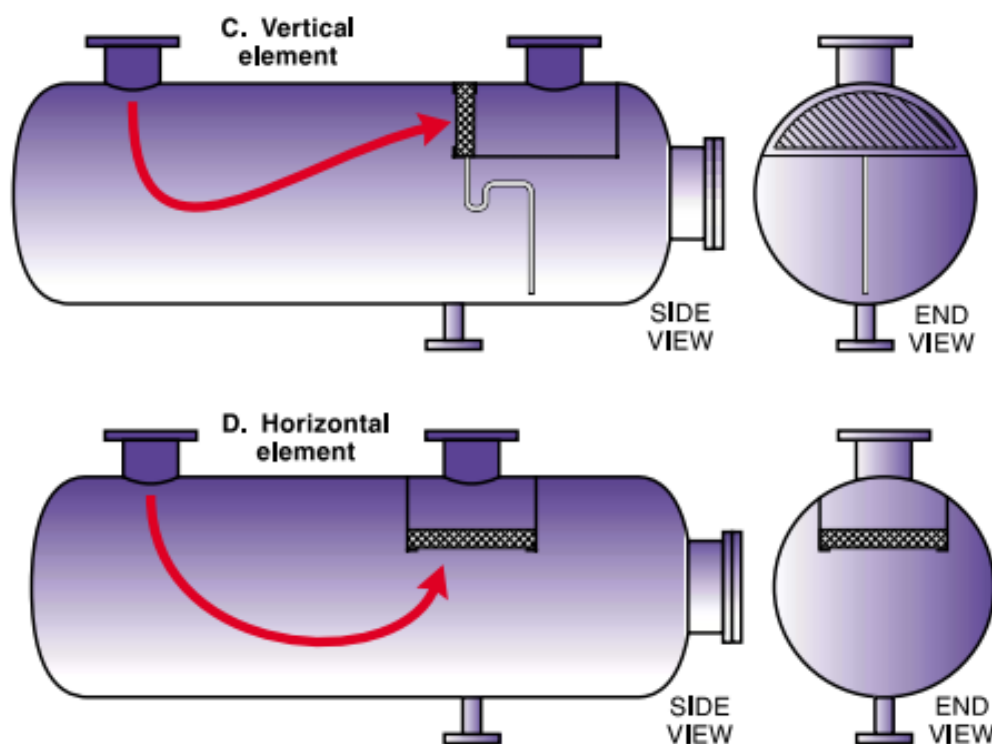


*Figure 2.3: Typical horizontal mist eliminator configurations [5], with friendly permission from AMACS*

The mechanism for droplet removal depends on the size of the droplets, which in turn is dependent on the process by which they were generated. For saturated vapor the droplet size is given between 3 and 20  $\mu\text{m}$  in diameter [5], which requires a really fine, knitted mesh for the separation process. The droplets collide and adhere to the mesh, aggregate to larger droplets and drain down from the mesh to the water outlets.

---

## 3 Theory

The behavior of every case of fluid flow in nature can be described by appropriate governing equations usually formulated as physical transport phenomena in the form of balances. In the literature, these equations are often referred to as NAVIER-STOKES equations, describing the motion of the flow, and the continuity equation. They are non-linear differential equations of second order and need to be solved numerically for most cases. However, there are solutions for certain problems assuming certain boundary conditions (e.g. POISEUILLE flow or COUETTE flow). In the following chapter, the governing equations are stated and shortly described.

Fluid flows in nature and industry are most often turbulent and so is the flow in mist eliminators. Therefore, turbulence must be taken into account as it has a major impact on the movement of the fluid and the pressure drop over the system. Turbulence can occur on the smallest length scales requiring very fine spatial discretization and thus making the computational effort quite large. For this reason turbulence models have been introduced modeling turbulence as a separate quantity besides momentum and mass. In chapter 3.2, turbulence models that were used to simulate the flow in the eliminator are discussed.

Since there is no analytical solution to the NAVIER-STOKES equations for most cases, numerical methods were developed in order to approximate a solution through an iterative process. Thereby, the mentioned balance calculations are performed over a control volume, referred to as a *cell*. These can be performed by hand, but for complex systems the usage of CFD is required, i.e. the equations are solved with an iterative solver on a computer. Some of the numerical aspects are shortly illustrated in chapter 3.3.

The wire mesh inside the eliminator was treated as a porous medium. Chapter 3.4 briefly describes the physical background and how it was implemented in the case study.

Most of the derivations and explanations in this chapter are based on ANDERSSON et al. [6], unless otherwise indicated.

### 3.1 Governing equations

The governing equations for a flow include the NAVIER-STOKES and the continuity equations. The former one describes the conservation of momentum, the latter one the conservation of mass. If heat transfer is involved, the conservation of energy also needs to be considered.

For this work, the EINSTEIN notation is used to formulate the governing equations according to [6]. The continuity equation for incompressible flow reads:

$$\frac{\partial U_i}{\partial x_i} = 0 \quad (3.1)$$

where  $U$  denotes velocity and  $x$  the spatial direction.

The assumption of incompressible flow was made throughout the paper, since the MACH number did not exceed a value of 0.3, as is elaborated in Chapter 4.1.3.

The NAVIER-STOKES equation, describing the conservation of momentum reads:

$$\frac{\partial U_i}{\partial t} + U_j \frac{\partial U_i}{\partial x_j} = -\frac{1}{\rho} \frac{\partial p}{\partial x_i} + \nu \frac{\partial}{\partial x_j} \left( \frac{\partial U_i}{\partial x_j} + \frac{\partial U_j}{\partial x_i} \right) + F_i \quad (3.2)$$

with  $t$  denoting the time,  $p$  denoting pressure,  $\nu$  as kinematic viscosity and  $F$  as combined body force. According to the EINSTEIN notation the index  $i$  denotes the spatial direction and  $j$  is the repeated index implying the summation of all terms in which it occurs twice. The kinematic viscosity  $\nu$  is defined as the quotient of dynamic viscosity  $\mu$  and density  $\rho$ :

$$\nu = \frac{\mu}{\rho} \quad (3.3)$$

## 3.2 Turbulence modeling

The flow inside the eliminator is assumed to be partly turbulent due to the high inlet and outlet velocities. Hence, some aspects of turbulence and its treatment in CFD are discussed in this chapter.

Turbulence is an unsteady, random and three dimensional movement of fluid particles within the main flow field encountered in nature as well as in many industrial processes. Therefore, turbulence is one major aspect which needs to be considered for engineering tasks involving fluid flows and is thus of great interest when CFD is applied. Principally, turbulence can be defined as the production and decay of dissipation [6]. The criterion for whether a flow has turbulent characteristics is the REYNOLDS number, which is the ratio of the inertial forces over the viscous forces:

$$Re = \frac{UL}{\nu} \quad (3.4)$$

where  $L$  denotes a characteristic length, e.g. the diameter of a pipe. Turbulent flow occurs at different  $Re$  numbers depending on the boundary conditions but for internal flows like in pipes the critical REYNOLDS number for the transition from laminar to turbulent flow is stated as  $Re \approx 2100$  [6].

The length and time scales of turbulent fluid flow are usually much smaller compared to the ones of the main flow field. Therefore, the turbulent movements require a much better resolution both regarding temporal and spatial discretization which can lead to very high computational costs. Thus, turbulence is usually described with a statistical method which is described in the following chapter.

### 3.2.1 REYNOLDS-averaged momentum and continuity equations

A common approach for the development of a turbulence model is based on the REYNOLDS-averaged NAVIER-STOKES (RANS) equations, for which the flow quantities are decomposed into a mean and a fluctuating component:

$$U_i = \overline{U_i} + U_i' \quad \& \quad p = \overline{p} + p' \quad (3.5)$$

For unsteady problems, ensemble averaging is used (see [7]). Applying this for Equations (3.1) and (3.2) gives the REYNOLDS decomposed continuity and momentum equations, which then can be averaged over time. Recalling the fact that the temporal average of a fluctuation is zero the RANS equations can be formulated as follows:

$$\frac{\partial \overline{U_i}}{\partial x_i} = 0 \quad (3.6)$$

$$\frac{\partial \overline{U_i}}{\partial t} + \overline{U_j} \frac{\partial \overline{U_i}}{\partial x_j} = -\frac{1}{\rho} \frac{\partial \overline{p}}{\partial x_i} + \nu \frac{\partial^2 \overline{U_i}}{\partial x_j \partial x_j} - \frac{\partial \overline{U_i U_j}}{\partial x_j} \quad (3.7)$$

Equation (3.7) can be rewritten using the dynamic viscosity and then the last term becomes  $-\rho \overline{U_i U_j} = \tau_{ij}$ , which is referred to as REYNOLDS stresses. It allows for a coupling between the mean flow and the fluctuations of the velocity field. It has the form of a symmetric tensor and thus introduces six new variables to the RANS equations, i.e. they are not closed anymore. Hence, turbulence models are used to introduce a closure.

Most turbulence models used in industry are based on the BOUSSINESQ approximation, which assumes that the components of the REYNOLDS stress tensor are proportional to the mean velocities of the flow field. It reads:

$$-\overline{U_i' U_j'} = \frac{\tau_{ij}}{\rho} = \nu_T \left( \frac{\partial \overline{U_i}}{\partial x_j} + \frac{\partial \overline{U_j}}{\partial x_i} \right) - \frac{2}{3} k \delta_{ij} \quad (3.8)$$

where  $k$  denotes the *turbulent kinetic energy*, which describes the intensity of the fluctuations around the mean flow velocity and is defined as follows:

$$k = \frac{1}{2} \overline{U'_i U'_i} \quad (3.9)$$

$\nu_T = \frac{\mu_T}{\rho}$  is referred to as the *kinematic turbulent* or *eddy viscosity*, which is used to model the REYNOLDS stresses. Hence, the BOUSSINESQ approximation assumes turbulent mass transport as a diffusive process and adds the eddy viscosity to the physical viscosity of the fluid.

Inserting Equation (3.8) into (3.7) gives the final form of the BOUSSINESQ approximation:

$$\frac{\partial \overline{U}_i}{\partial t} + \overline{U}_j \frac{\partial \overline{U}_i}{\partial x_j} = -\frac{1}{\rho} \frac{\partial \overline{p}}{\partial x_i} - \frac{2}{3} \frac{\partial k}{\partial x_i} + \frac{\partial}{\partial x_j} \left[ (\nu_T + \nu) \left( \frac{\partial \overline{U}_i}{\partial x_j} + \frac{\partial \overline{U}_j}{\partial x_i} \right) \right] \quad (3.10)$$

Further assumptions made by the BOUSSINESQ approximation are the isotropy of turbulence and the existence of equilibrium between stress and strain. Mainly the former one can cause problems if the flow is strongly anisotropic, e.g. close to walls or in cyclonic streams [6].

Like the normal viscosity, the turbulent viscosity can be expressed by a length and a velocity:

$$\nu_T = C_v \frac{l^2}{t} = C_v U l \quad (3.11)$$

Where  $l$  contributes for the length scale of the turbulent eddies and  $U$  for the velocity they travel with.  $C_v$  is a scaling factor usually obtained from experiments. The calculation of these two parameters by the use of additional transport equations is the purpose of turbulence modeling. Depending on the number of transport equations added, it can be distinguished between zero-, one- or two-equation models.

The models used during the simulation of the mist eliminator were two-equation models commonly applied in industry, namely the  $k$ - $\varepsilon$  model and the  $k$ - $\omega$ -SST model, and are discussed in the following sections. Further, the SPALART-ALLMARAS model was used as a representative of the one-equation models.

#### 3.2.2 The $k$ - $\varepsilon$ model

The  $k$ - $\varepsilon$  model uses the turbulent kinetic energy  $k$  to model the velocity and the turbulent dissipation rate  $\varepsilon$  to model the length scale. It is one of the most common turbulence models and an established industry standard. The eddy viscosity is calculated as follows:



$$\nu_T = C_\mu \frac{k^2}{\varepsilon} \quad (3.12)$$

The proportional factor was set to  $C_\mu = 0.09$ , which is a common value used in industry. The turbulent dissipation  $\varepsilon$  which is the rate at which the turbulent kinetic energy is converted into heat is defined as:

$$\varepsilon = \nu \frac{\overline{\partial U_i \partial U_i}}{\partial x_j \partial x_j} \quad (3.13)$$

To estimate  $k$  and  $\varepsilon$  two additional transport equations need to be formulated:

$$\frac{\partial k}{\partial t} + \overline{U_j} \frac{\partial k}{\partial x_j} = \nu_T \left[ \left( \frac{\partial \overline{U_i}}{\partial x_j} + \frac{\partial \overline{U_j}}{\partial x_i} \right) \frac{\partial \overline{U_i}}{\partial x_j} \right] - \varepsilon + \frac{\partial}{\partial x_j} \left[ \left( \nu + \frac{\nu_T}{\sigma_k} \right) \frac{\partial k}{\partial x_j} \right] \quad (3.14)$$

for the turbulent kinetic energy  $k$  and:

$$\frac{\partial \varepsilon}{\partial t} + \overline{U_j} \frac{\partial \varepsilon}{\partial x_j} = C_{\varepsilon 1} \nu_T \frac{\varepsilon}{k} \left[ \left( \frac{\partial \overline{U_i}}{\partial x_j} + \frac{\partial \overline{U_j}}{\partial x_i} \right) \frac{\partial \overline{U_i}}{\partial x_j} \right] - C_{\varepsilon 2} \frac{\varepsilon^2}{k} + \frac{\partial}{\partial x_j} \left[ \left( \nu + \frac{\nu_T}{\sigma_\varepsilon} \right) \frac{\partial \varepsilon}{\partial x_j} \right] \quad (3.15)$$

for the turbulent dissipation rate  $\varepsilon$ . Recommended values for the model coefficients are  $C_{\varepsilon 1} = 1.44$ ,  $C_{\varepsilon 2} = 1.92$ ,  $\sigma_k = 1.00$  and  $\sigma_\varepsilon = 1.30$ , which were obtained from experiments and can be changed manually for the most CFD software. Several simplifications and closures have been used to obtain Equations (3.14) and (3.15), which will not be discussed in detail here but are further explained in [7]. Three equations have been stated for the three variables, namely turbulent kinematic viscosity, dissipation rate and kinetic energy, and thus a closure is obtained.

The  $k$ - $\varepsilon$  model is stated to have numerical robustness and to give good results for free-shear layer flows with relatively small pressure gradients [8]. It was originally developed to simulate flows with a very high REYNOLDS number. However, for problems involving adverse pressure gradients, swirling flows and strong streamline curvature it gives poorer results [6]. Furthermore, for regions close to walls, damping functions have to be used.

Because of its robustness, this model was used for the first simulations of the eliminator flow.

### 3.2.3 The $k$ - $\omega$ -SST model

The following explanations are mainly based on [9].

Another two-equation model widely used in industry is the  $k$ - $\omega$ -SST model (Shear Stress Transport model), which expresses the eddy viscosity by the turbulent kinetic energy and a *specific dissipation* which is defined as:

$$\omega = \frac{\varepsilon}{k} \quad (3.16)$$

This model was used for most of the simulations in this project and is thus explained in more detail. The  $k$ - $\omega$ -SST model combines the advantages of the  $k$ - $\varepsilon$  model and the  $k$ - $\omega$  model, which is stated to have better properties in regions close to walls [6]. Therefore, the incompressible  $k$ - and  $\omega$ -equations are stated first:

$$\frac{\partial k}{\partial t} + \overline{U_j} \frac{\partial k}{\partial x_j} = \frac{\tau_{ij}}{\rho} \frac{\partial \overline{U_i}}{\partial x_j} - \beta^* \omega k + \frac{\partial}{\partial x_j} \left[ (\nu + \sigma_k \nu_T) \frac{\partial k}{\partial x_j} \right] \quad (3.17)$$

for the turbulent kinetic energy  $k$  and:

$$\begin{aligned} \frac{\partial \omega}{\partial t} + \overline{U_j} \frac{\partial \omega}{\partial x_j} = & \frac{\gamma}{\nu_T} \frac{\tau_{ij}}{\rho} \frac{\partial \overline{U_i}}{\partial x_j} - \beta \omega^2 + \frac{\partial}{\partial x_j} \left[ (\nu + \sigma_\omega \nu_T) \frac{\partial \omega}{\partial x_j} \right] \\ & + 2(1 - F_1) \frac{\sigma_{\omega 2}}{\omega} \frac{\partial k}{\partial x_j} \frac{\partial \omega}{\partial x_j} \end{aligned} \quad (3.18)$$

for the specific dissipation  $\omega$ , which is the inverse of the turbulent dissipation timescale. The quotient containing the shear stress tensor  $\frac{\tau_{ij}}{\rho}$  can be calculated according to the BOUSSINESQ approximation. The turbulent kinematic viscosity is here defined as:

$$\nu_T = \frac{a_1 k}{\max(a_1 \omega, SF_2)} \quad (3.19)$$

with the strain invariant  $S$  as:

$$S = \sqrt{S_{ij} S_{ij}} \quad (3.20)$$

where

$$S_{ij} = \frac{1}{2} \left( \frac{\partial \bar{U}_i}{\partial x_j} + \frac{\partial \bar{U}_j}{\partial x_i} \right) \quad (3.21)$$

The model distinguishes between different regions based on their distance  $d$  from the closest wall and uses either a more  $k$ - $\varepsilon$  or a more  $k$ - $\omega$  similar approach to solve the flow field. This is controlled by the blending factors  $F_1$  and  $F_2$ :

$$F_1 = \tanh \left[ \left( \min \left[ \max \left( \frac{\sqrt{k}}{\beta^* \omega d}, \frac{500\nu}{d^2 \omega} \right), \frac{4\sigma_{\omega 2} k}{CD_{k\omega} d^2} \right] \right)^4 \right]$$

$$F_2 = \tanh \left[ \left( \max \left( \frac{2\sqrt{k}}{\beta^* \omega d}, \frac{500\nu}{d^2 \omega} \right) \right) \right] \quad (3.22)$$

$$CD_{k\omega} = \max \left( 2\sigma_{\omega 2} \frac{1}{\omega} \frac{\partial k}{\partial x_j} \frac{\partial \omega}{\partial x_j}, 10^{-10} \right)$$

The closure constants recommended in the literature and used for this project are given in Table 3.1.

Table 3.1: Closure constants for the  $k$ - $\omega$ -SST model [9]

$k$ - $\omega$ closure	$\sigma_{k1}$	0.85
	$\sigma_{\omega 1}$	0.65
	$\beta_1$	0.075
$k$ - $\varepsilon$ closure	$\sigma_{k2}$	1.00
	$\sigma_{\omega 2}$	0.856
	$\beta_2$	0.0828
SST closure	$\beta^*$	0.09
	$a_1$	0.31
	$\gamma_1$	$\frac{5}{9}$
	$\gamma_2$	0.44

The constants occurring in the equations above without a numbering index (e.g.  $\beta$  or  $\sigma_k$ ) are blended with the following equation where  $\phi$  represents the corresponding constant:

$$\phi = F_1 \phi_1 + (1 - F_1) \phi_2 \quad (3.23)$$

Now, the closure for the model is complete. A limiter for the production term in the  $k$ -equation is usually used, which replaces the term  $\frac{\tau_{ij}}{\rho} \frac{\partial \bar{U}_i}{\partial x_j}$  with:

$$\min\left(\frac{\tau_{ij}}{\rho} \frac{\partial \bar{U}_i}{\partial x_j}, 20\beta^* \omega k\right) \quad (3.24)$$

As can be seen, the  $k$ - $\omega$ -SST model is more complex than the  $k$ - $\varepsilon$  model since two sets of equations need to be calculated first and then the more suitable one is chosen for the appropriate flow region. The model uses the  $k$ - $\omega$  model for boundary layers and switches to  $k$ - $\varepsilon$  behavior in the free stream regions of the flow domain. This also means that no damping function close to walls is required. Because of its practical characteristics, the  $k$ - $\omega$ -SST model became very popular in industry. However, it is stated to need slightly more computation time than either of the models it is based on and to over predict turbulence in regions with large normal strain, e.g. with high accelerations [6].

Since several authors (e.g. [6], [10]) state this model to be very accurate for complex geometries and due to the benefits of combining two turbulence models, the  $k$ - $\omega$ -SST model was used for most of the simulations during this project.

#### 3.2.4 The SPALART-ALLMARAS model

In contrast to the models discussed before, the SPALART-ALLMARAS model uses only one transport equation to calculate the eddy viscosity. It was originally developed for external aerodynamics of streamlined bodies [9]. In OpenFOAM the following version of this model is used:

$$\begin{aligned} \frac{\partial \tilde{\nu}}{\partial t} + \bar{U}_j \frac{\partial \tilde{\nu}}{\partial x_j} = & c_{b1}(1 - f_{t2})\tilde{S}\tilde{\nu} - \left[ c_{w1}f_w - \frac{c_{b1}}{\kappa^2} f_{t2} \right] \left( \frac{\tilde{\nu}}{d} \right)^2 \\ & + \frac{1}{\sigma} \left[ \frac{\partial}{\partial x_j} \left( (\nu + \tilde{\nu}) \frac{\partial \tilde{\nu}}{\partial x_j} \right) + c_{b2} \frac{\partial \tilde{\nu}}{\partial x_i} \frac{\partial \tilde{\nu}}{\partial x_i} \right] \end{aligned} \quad (3.25)$$

The turbulent viscosity is here defined as:

$$\nu_T = \tilde{\nu} f_{\nu 1} \quad (3.26)$$

The closures and values for the individual model coefficients were taken from [10].

Since only one equation needs to be solved, the computational time is lower compared to the other two models described above, hence it was also tested for the eliminator flow.

## 3.3 Discretization

The governing equations (3.1) and (3.2) can most often not be solved analytically. Thus, numerical methods are used to obtain results in an iterative process, which require discreti-

zation for the continuous quantities. In the OpenFOAM programmer's guide [11] the discretization process is divided into:

“Spatial discretisation defining the solution domain by a set of points that fill and bound a region of space when connected;

Temporal discretisation (for transient problems) dividing the time domain into [...] a finite number of time intervals, or steps;

Equation discretisation generating a system of algebraic equations in terms of discrete quantities defined at specific locations in the domain, from the PDEs that characterise the problem.”

### 3.3.1 Spatial discretization

Spatial discretization in OpenFOAM is usually performed with a hexahedral mesh, which can be refined and also be snapped to a non-hexahedral boundary. Figure 3.1 shows two neighboring cells and their parameters.  $P$  denotes the center of the current cell,  $f$  the internal cell face and  $N$  is the center of the next cell.  $d$  is the length vector between  $P$  and  $N$ .  $S_f$  is the surface area vector.

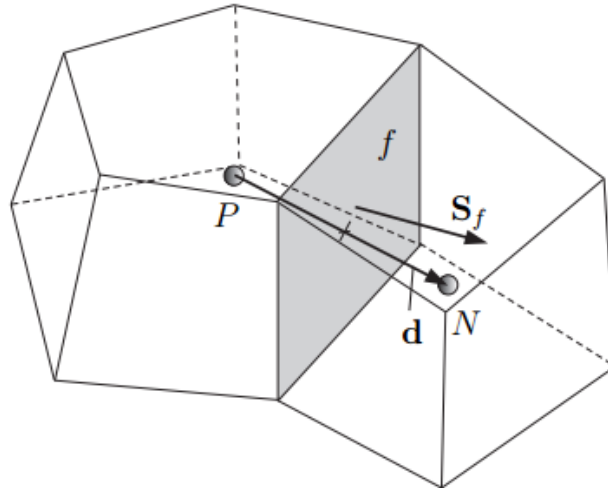


Figure 3.1: Two neighboring finite volumes (cells) [11]

The nomenclature from Figure 3.1 is used to describe the discretization of the governing equations in the next chapter.

### 3.3.2 Discretization of the governing equations

The individual terms of the governing equations can be discretized by different discretization schemes offered in OpenFOAM. Usually the GAUSS divergence theorem is used for the integration of the individual terms which states that the net flux through a surface is the sum of all sinks and sources inside a volume surrounded by that surface. Alternatively,

OpenFOAM offers higher order schemes like the least squares method for gradients, but for this work only GAUSS integration in combination with an interpolation scheme was used. The individual integration process for each term of the governing equations can be found in [6].

After the integration process the interpolation scheme needed to be specified. In the first simulations, GAUSS integration with a limited linear interpolation scheme was used for discretization. It can also be interpreted as a bounded version of the *central differencing scheme* (CDS) and is second order accurate. The arbitrary field entity  $\phi$  is interpolated via linear interpolation as follows:

$$\phi_f = \phi_P \lambda_f + \phi_N (1 - \lambda_f) \quad (3.27)$$

with  $\lambda_f$  as the ratio of the distances from  $f$  to  $N$  and  $P$  to  $N$ . This scheme becomes unstable if the problem involves highly convective flows. Thus, the SWEBY limiter was used in order to bind the CDS preventing it from too high oscillations (see [12]).

Another scheme which was used in this project was the *upwind scheme*. It assumes the face value between two cells as equal to the nearest upstream cell, i.e.:

$$\phi_f = \phi_P \text{ if } S_f \cdot U_f \geq 0 \quad \text{or} \quad \phi_f = \phi_N \text{ if } S_f \cdot U_f < 0 \quad (3.28)$$

It is the only scheme which is purely bounded. Also, a combination of both schemes - the *linear upwind scheme* - was used for some of the divergence terms, which switches between upwind differencing (UD) and CDS with a blending factor:

$$\phi_f = \phi_{fUD} + \psi(\phi_{fCD} - \phi_{fUD}) \quad (3.29)$$

which for  $\psi = 1$  is purely a CDS and for  $\psi = 0$  is purely an upwind scheme. The user can specify the blending factor by a parameter in the case files, which was left default during this project.

For the time derivative the EULER implicit method was used, which is first order accurate and bounded. Applying this scheme, the accumulation term becomes:

$$\frac{\delta}{\delta t} \int_V \phi dV = \frac{(\phi_P V)^n - (\phi_P V)^o}{\Delta t} \quad (3.30)$$

where  $n$  denotes for the new values at the time step which is solved for and  $o$  denotes old values from the previous time step.

### 3.3.3 Temporal discretization

Temporal discretization involves the discretization of the governing equations for transient problems. Using the EULER implicit method gives for the time derivative:

$$\int_t^{t+\Delta t} \left[ \frac{\partial}{\partial t} \int_V \phi dV \right] dt = \int_t^{t+\Delta t} \frac{(\phi_P V)^n - (\phi_P V)^o}{\Delta t} dt = \frac{(\phi_P V)^n - (\phi_P V)^o}{\Delta t} \Delta t \quad (3.31)$$

and for the spatial derivatives:

$$\int_t^{t+\Delta t} \left[ \int_V \phi dV \right] dt = \int_t^{t+\Delta t} \phi dt = \phi^n \Delta t \quad (3.32)$$

This scheme is bounded, unconditionally stable and first order accurate. Other schemes such as CRANK-NICOLSON or backwards differencing are available in OpenFOAM but were not applied during this project. They are further discussed in [7] and [11].

## 3.4 Treatment of a porous wire mesh

The wire mesh which is used to separate the droplets from the steam (see Chapter 2.2.2) was modeled as a porous medium. Such a medium can be defined as a material partially consisting of solids and pores, which are filled with a fluid. Its most important property is the *porosity*  $\vartheta$  which is defined as the fraction of the pores  $V_V$  over the total volume  $V_T$  of the medium:

$$\vartheta = \frac{V_V}{V_T} \quad (3.33)$$

The flow through porous media can be described by adding a sink term to the governing equations [13]:

$$\frac{\partial}{\partial t}(\vartheta U_i) + U_j \frac{\partial U_i}{\partial x_j} = -\frac{\partial p}{\partial x_i} + \nu \frac{\partial}{\partial x_j} \left( \frac{\partial U_i}{\partial x_j} + \frac{\partial U_j}{\partial x_i} \right) + F_i + \frac{S_i}{\rho} \quad (3.34)$$

The sink  $\frac{S_i}{\rho}$  consists of a viscous loss term and an inertial loss term leading to a pressure drop proportional to the flow velocity and its square. For a simple homogeneous porous medium it can be expressed by the DARCY-FORCHHEIMER law:

$$\frac{S_i}{\rho} = \frac{dp}{\rho dx_i} = - \left( \nu d_i + \frac{1}{2} |U| f_i \right) U_i \quad (3.35)$$

In OpenFOAM, a porous medium is defined by a cell zone within the flow domain, for which the DARCY coefficient  $d_i$  and the FORCHHEIMER coefficient  $f_i$  need to be specified. These parameters determine the flow resistance through the medium and thus the pressure drop.

The latter one was provided by the manufacturer and used to calculate the FORCHHEIMER coefficient, while the DARCY coefficient was neglected. This approach seemed reasonable since the FORCHHEIMER term accounts for inertial effects caused by high velocities within in the filter.



---

## 4 Case study

The case study was divided into three stages. First, the right simulation setup had to be established. Usually, this is done by comparing the simulation results of the present design to measured data, in order to validate the modeling procedure. Several cases were run to identify an appropriate simulation setup including a mesh sensitivity analysis as well as the testing of different turbulence models and numerical schemes. From this procedure the simulation which fits best to the measurements would be used as basis of comparison. However, for this project only one parameter for validation could be provided by the manufacturer, namely the pressure drop over the filter. As it turned out, most of the simulations calculated the pressure drop rather accurately with a deviation of  $\pm 5\%$ , thus other criteria needed to be considered based on suggestions and recommendations found in the literature.

After an appropriate simulation setup was found, the first investigations regarding the operation conditions could be made. This included the variation of the inlet boundary conditions, i.e. a different distribution of the flow into the eliminator. Three different cases were tested during this part of the project.

The last step was the change of the geometry in order to find an improved design with a lower global pressure drop, since this is one of the desired improvements for future eliminator designs. Further, the flow within the filter is important for the separation efficiency and a more even velocity distribution is usually desirable. Besides the current design, two additional ones were modeled and simulated in OpenFOAM.

### 4.1 Modeling of the current mist eliminator design

The following chapter describes the pre-processing for the current eliminator design used by Verkís at e.g. Reykjanes Geothermal Power Plant. All further simulations were prepared in a similar way and only the differences to the initial case setup are explained.

#### 4.1.1 Geometry creation

The current mist eliminator used by Verkís has two horizontal inlets at the side caps and three vertical outlet pipes, which are connected to a bigger horizontal one, called gathering pipe. The filter is located in the center of the eliminator below the outlet pipes. Furthermore, two water outlets at the bottom are used to drain the drum.

For the simulations, the model had to be simplified in order to ease the mesh generation and to enhance numerical convergence. First, the openings on the side were excluded,

since they are closed during operation and are only used for maintenance. This was also the case for the valves and openings at the water outlets. All edges reaching into the flow domain, for example, pipe endings were not included. An exception was the shroud holding the filter, which was modeled as a baffle, i.e. as a surface with the characteristics of a wall boundary condition. The wire mesh itself was modeled as a porous medium specified as a cell zone within the flow domain. Additionally, internal surfaces, which have no impact on the flow behavior, were included for the purpose of post-processing.

The CAD software used for this project was *Autodesk Inventor 2014 Professional*. A 3D-model of the eliminator geometry utilized for the initial simulations is depicted in Figure 4.1. The length of the inlets was increased to allow for the development of a fully turbulent velocity profile when the flow enters the drum. Another measure to achieve such a profile was the usage of mapped patches, as will be discussed in Chapter 4.1.3. Also, the horizontal outlet pipe was increased in length to avoid backflow into the drum and thus repercussions, i.e. the flow field inside the drum was intended to be independent of the flow in the outlet pipe.

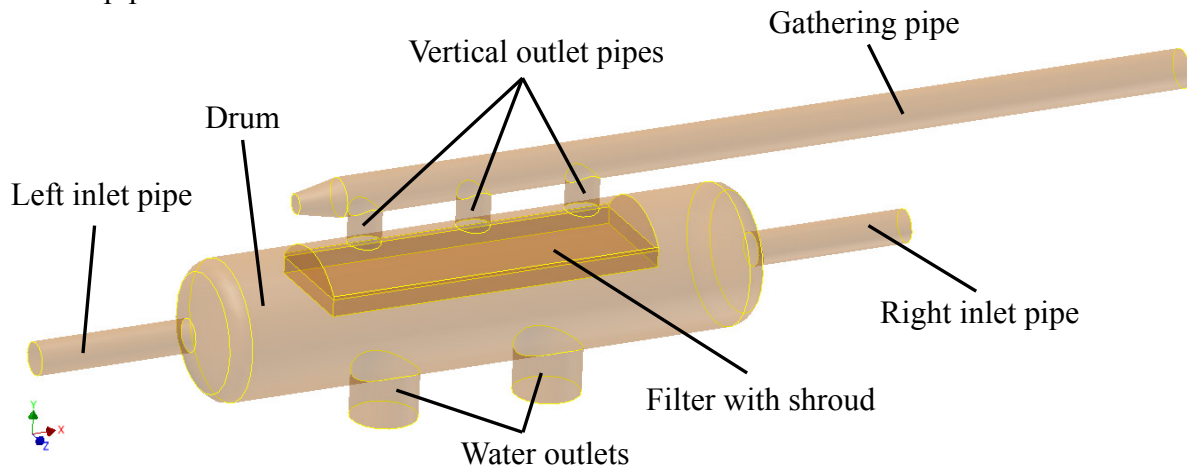


Figure 4.1: 3D-model of the internal volume of the mist eliminator

After the 3D-model was created in Inventor it was exported as .step-file (*"Standard for the Exchange of Product model data"*) in order to make it usable in *Salome* – a freely available pre-processor employed for geometry manipulation and mesh generation. In *Salome*, the patches and faces were grouped and named according to their functionality and the usual OpenFOAM naming convention (capital letters to separate words).

The steel sheet surrounding the flow domain was defined as a wall. The inlets and outlets were defined as patches and confined the flow domain with in- and outflow boundary conditions. The shroud was defined as a baffle separating the region before the filter from the one after the filter, so that the flow was forced through the wire mesh. Three internal faces were used to observe the flow through the filter. One face was used for the gathering outlet pipe and three additional ones for the outlet pipes. An overview of all patches and faces is given in Table 4.1 and Figure 4.2.

Table 4.1: Name convention and functionality of patches and faces used for the mist eliminator models

Patch/face name	Functionality
mistEliminator	wall confining the flow domain
shroud	baffle separating the regions before and after the filter
inletLeft inletRight	inflow from each side of the domain
outlet	outflow from the domain; end of the gathering pipe
porousIn porousMid porousOut	internal faces confining/intersecting the filter; used for post-processing
pipeLeft pipeMid pipeRight	internal faces located 0.8 m downstream from the filter intersecting the three vertical outlet pipes; used for post-processing
outletXSec	internal face located 1.5 m upstream from the outlet intersecting the horizontal gathering pipe; used for post-processing

After grouping the patches and naming them they were exported as .stl-files (“*Standard Tessellation Language*”), which then could be used for meshing in OpenFOAM. This procedure was performed in a similar way for all the following designs.

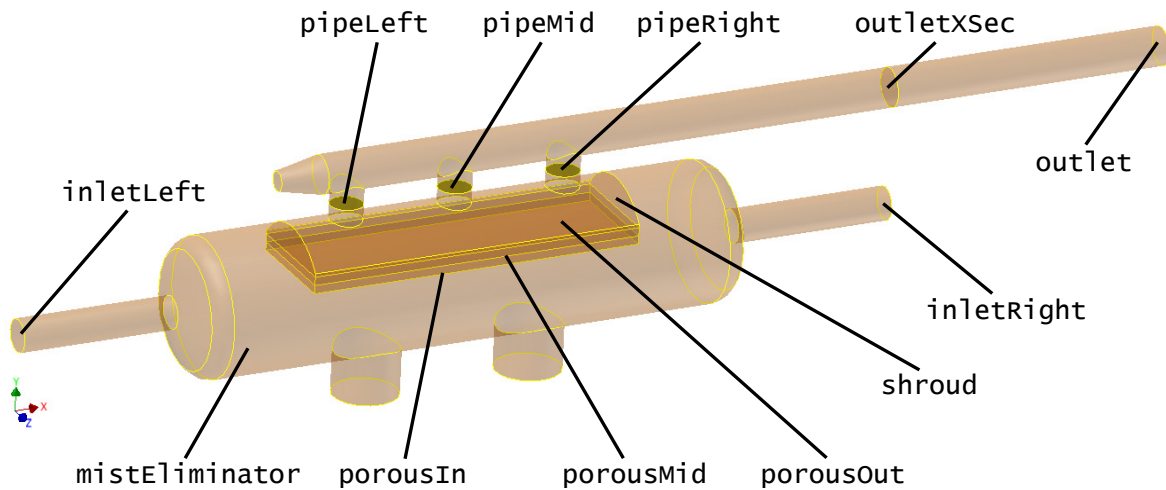
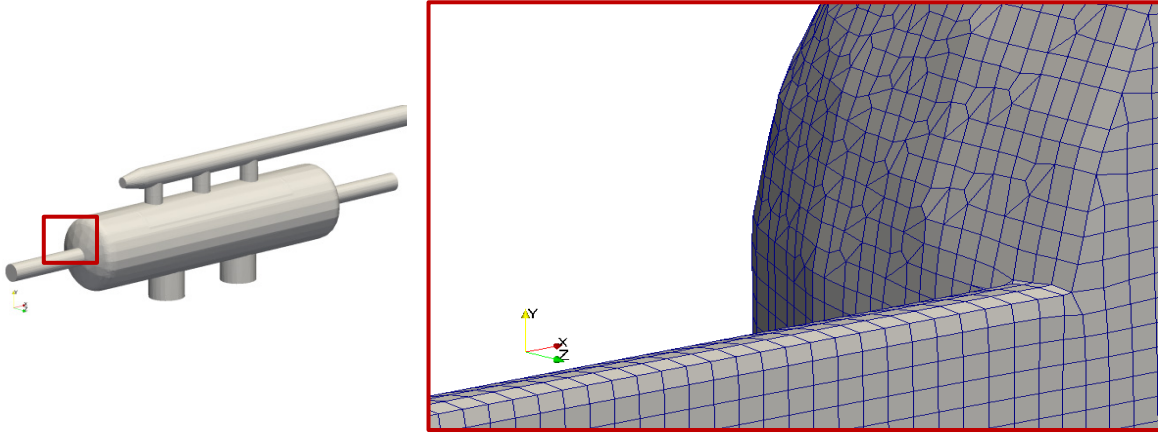


Figure 4.2: Overview of patches used for modeling and post-processing

#### 4.1.2 Meshing

The mesh for spatial discretization was created with the OpenFOAM utilities `blockMesh` and `snappyHexMesh`. With the former one a rectangular block consisting of hexahedral cells large enough to contain the eliminator geometry was created. The initial cell size, i.e. the dimensions of the individual hexahedrons, was specified in the `blockMesh` dictionary

as 50x50x50 mm. Next, snappyHexMesh was used to snap the mesh to the patches defined in Table 4.1. During this process, the utility created a castellated mesh by splitting the cells at the edges of the geometry into smaller ones in order to approximate the curvature of the surface. Then, cells, which were located outside the closed geometry were removed, followed by surface snapping, during which the castellated mesh was smoothened. For a detailed description of the snapping process the reader is referred to the OpenFOAM user guide [14]. The meshed geometry is illustrated in Figure 4.3. The overall number of cells obtained was 449,000.



*Figure 4.3: Solid eliminator geometry (left) and a mesh cross section (right)*

For the meshing of the eliminator no boundary layer refinement was employed due to very high REYNOLDS numbers in the order of  $Re \approx 37.6 \cdot 10^6$ . This would have led to very fine cells close to the walls with a thickness of less than one millimeter. The incorporation of such small boundary layers would have increased the computational time significantly and could thus not be realized within the given timeframe. However, future investigations should take an appropriate wall treatment into account. The calculation of the parameters describing the wall region can be found in Appendix A.

### 4.1.3 Boundary conditions

For all of the case setups, the boundary conditions of the non-internal patches were defined according to their functionality listed in Table 4.1 and to the corresponding variable. In OpenFOAM, the specification of the BCs is carried out for each flow entity, i.e. for the first simulation the velocity and the pressure as well as the turbulent kinetic energy, dissipation rate and eddy viscosity had to be specified. The  $k$ - $\epsilon$  model was chosen for the first simulation, since it is stated to be robust and suitable for high  $Re$ -numbers as discussed in Chapter 3.2.2. The velocity and pressure BCs are listed in Table 4.2 and Table 4.3. For the calculation of the corresponding values and the estimation of the turbulent inlet properties, which were implemented similarly to the velocity BCs, the reader is referred to Appendix B.

Table 4.2: Velocity BCs for the initial simulation setup

Patch/face name	value/info
mistEliminator	(0 0 0) m/s, wall
inletLeft	(16 0 0) m/s, mapped
inletRight	(-16 0 0) m/s, mapped
outlet	zero gradient

Table 4.3: Pressure BCs for the initial simulation setup

Patch/face name	value/info
mistEliminator	zero gradient, wall
inletLeft	zero gradient
inletRight	zero gradient
outlet	0 Pa

As can be seen in the mentioned tables, the inlets were defined as velocity inlets, i.e. a flow of constant velocity streamed into the domain perpendicularly to the inlet patches. For the walls, the *no-slip condition* was used stating that the relative velocity at walls is zero. The outlet was defined as a pressure outlet with a value of 0 Pa, i.e. all pressures were calculated as relative pressures. Another assumption regarding the pressure was incompressibility, since the MACH number was significantly below 0.3, i.e. the lower limit from which point on effects caused by compression should be taken into account. The working pressure in the eliminator was given at 20 bar-a, which for saturated steam corresponds to a speed of sound of 505 m/s. The highest velocities encountered during the simulations were about 37 m/s, thus the assumption of incompressibility seemed valid.

Another problem, which needed to be considered was turbulent inflow. The flow inside the eliminator was assumed to be turbulent, thus the velocity entering the drum should have a fully turbulent profile. This aspect was incorporated by the usage of *mapped patches* one meter downstream from the inlets. The mapped quantities were used as new inlet conditions for each time step, thus a turbulent flow could establish after a certain amount of simulated time. Figure 4.4 shows the velocity profile over the cross section of one of the inlet pipes with and without mapping.

## 4.1 Modeling of the current mist eliminator design

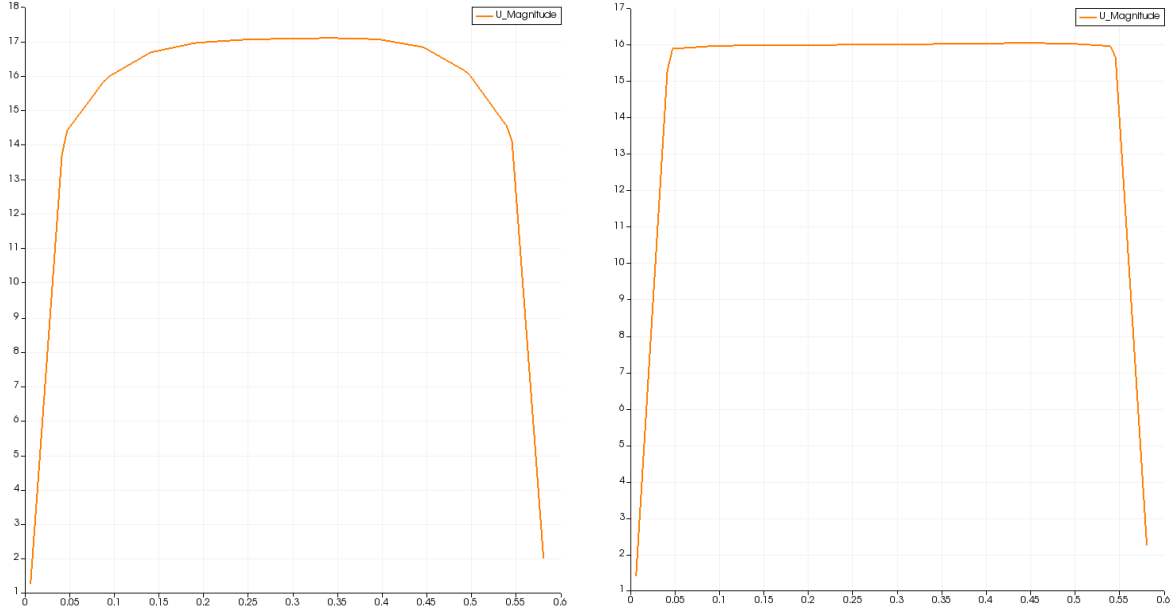


Figure 4.4: Velocity profile in one inlet pipe with (left) and without mapping (right)

The wire mesh was modeled as a porous zone, which adds a source term to the governing equations as shown in Equation (3.34). For this project it was modeled as an `explicitPorositySource` which uses the Darcy-Forchheimer law and requires the input of the corresponding coefficients. As mentioned in Chapter 3.4, only the FORCHHEIMER coefficient was used to express the source term which is calculated in Appendix C as  $f_i = 251.31$ . Since the filter consists of arbitrarily arranged wires, it was assumed that the flow resistance has the same value for all three spatial dimensions, hence  $f_1 = f_2 = f_3 = f_i$ .

The droplets were assumed to be very small by weight and volume ( $d \leq 20 \mu\text{m}$ ) and thus the flow in this project was treated as a single-phase problem. This simplification has to be verified by two-phase flow models and/or measurements in future projects.

### 4.1.4 Discretization schemes

As already stated in Chapter 3.3.2, the schemes used for this work were GAUSS integration combined with the limited linear, the upwind and/or the linear upwind scheme. For the first simulation linear schemes and their variants were used, which are second-order accurate. For the divergence terms the limited linear scheme was chosen, since it is stated to be very stable due to its bounding limiter. For the gradient terms the simple linear scheme and for the LAPLACIAN terms the linear scheme with orthogonal correction were chosen.

The implicit EULER scheme was selected for the temporal discretization, which is first order accurate, bounded and unsteady. Theoretically this scheme should allow for COURANT numbers greater than 1, however, the simulation became unstable for values over  $\approx 3$ . The reason for that was the selected transient solver `piSoFoam`, which can operate for COURANT

numbers only slightly over 1. Thus, the time step was kept rather small. The COURANT number describes how many cells the flow travels during one time step and can be calculated for strong convection by the following equation:

$$CFL = \frac{\Delta t U}{\Delta x} \quad (4.1)$$

It is recommended to start the simulations with a rather low COURANT number, so Equation (4.1) was used, to estimate the time step. With the COURANT number set to 1, an assumed minimum cell size of 10 mm and maximum velocity of 25 m/s, the time step would be 0.4e-3 s, which was used throughout the project.

To allow the flow to fully develop and to account for the larger turbulent timescales the overall simulated time had to be chosen appropriately. If the solution converges in time, i.e. if certain flow patterns show a repetitive character, the simulation time might be decreased. For the initial case it was chosen to be 25 s.

As it turned out, the first simulation could be run with the configurations explained in the last three chapters and gave good agreement with the pressure drop value over the filter stated by the manufacturer. However, to assure that the solution is independent of the simulation properties, the mesh, the numerical schemes and the turbulence model were changed according to literature recommendations and experience. The variables for comparison as well as the different variants of case setups are discussed in the following chapters.

## 4.2 Simulation variants

In total, eleven simulations were performed during this project, which can be divided into three categories:

1. Influence of the simulation setup
2. Change of boundary conditions
3. Change of geometry

The first category investigated the dependency of the results on properties concerning mesh quality, turbulence model, numerical schemes and temporal discretization. For the simulations of the second category, the mass flow distribution for the inlets was changed, i.e. different inlet velocities were specified. The last simulations were run with modified inlet and outlet configurations. Each case is described in the following chapters and some results are briefly mentioned if needed, however, a detailed evaluation of each case is given in Chapter 5. An overview of all simulation variants can be found at the end of the chapter in Table 4.5.

### 4.2.1 Influence of the simulation setup

To find the setup, which best approximates the given measurement data and to investigate on the sensitivity of the results towards simulation parameters, certain simulation properties were varied, namely the cell size, the turbulence model and the numerical scheme.

- **Cell size**

In order to ensure that the results obtained from the simulations are grid independent, three simulations with different cell sizes were performed for the original design described in Chapter 4.1. For the first and the second simulation, only the global cell size was changed in the `blockMeshDict`, but for the last one a region for refinement was specified. This region included the filter and a cylinder containing the jet streams originating from the inlets. The simulations were named according to the OpenFOAM naming convention and are listed with their corresponding properties in Table 4.4.

*Table 4.4: Mesh properties for the mesh sensitivity analysis*

Simulation	Cell size	Number of cells
<code>originalCoarse</code>	80 mm	109,000
<code>originalMedium</code>	50 mm	449,000
<code>originalRefined</code>	50 mm, 25 mm for refined regions	945,000

The meshes used for the mesh sensitivity analysis are illustrated in the figures below by a xy-cross-section.

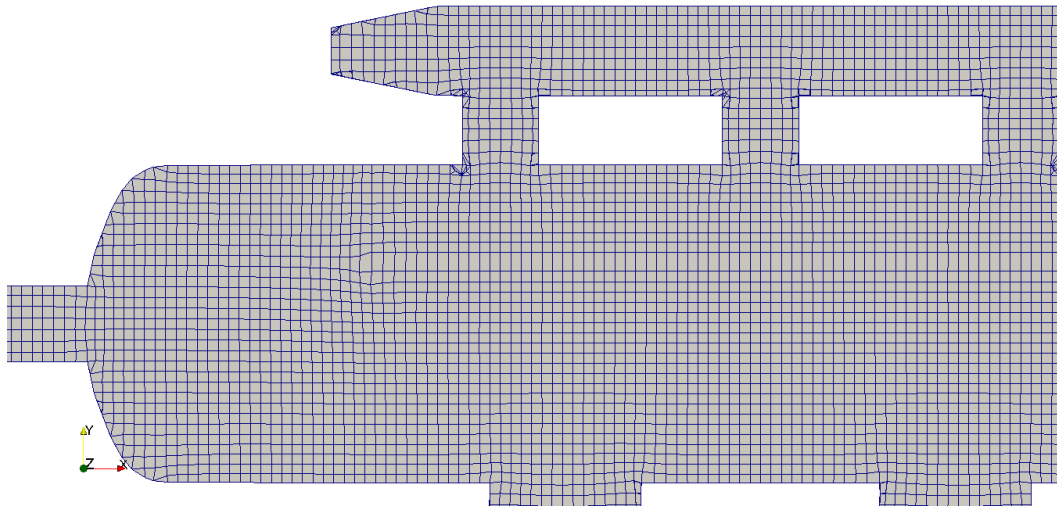


*Figure 4.5: Mesh xy-cross-section of the case `originalCoarse`*



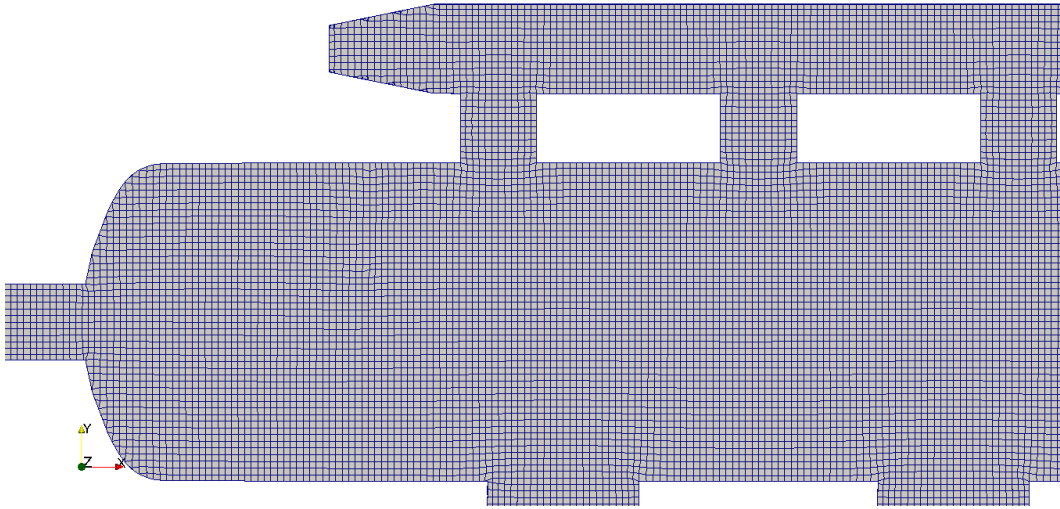


Figure 4.6: Mesh *xy*-cross-section of the case *originalMedium*

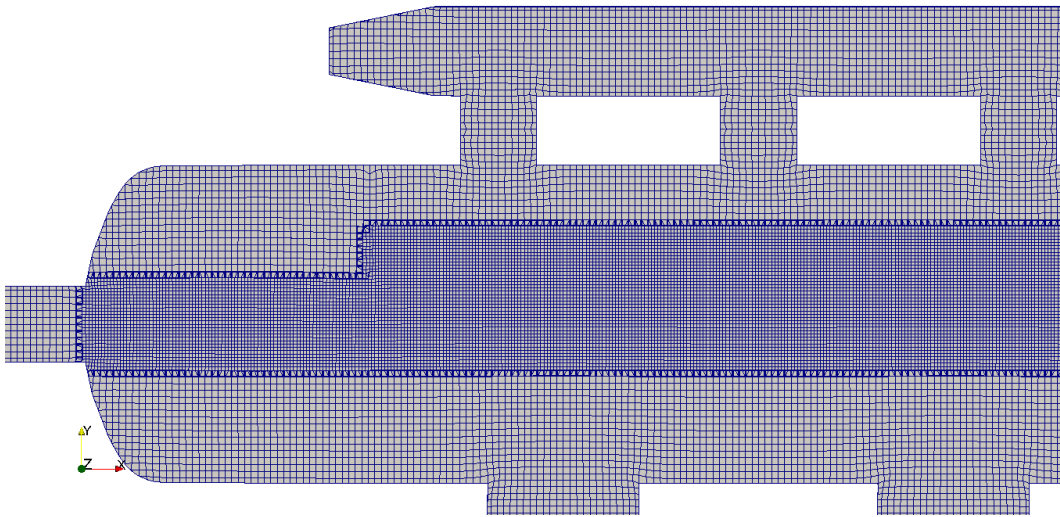


Figure 4.7: Mesh *xy*-cross-section of the case *originalRefined*

The results showed that the difference between the medium and the refined case is rather small, thus the following simulations were performed with a cell size of 50 mm.

- **Numerical schemes**

The stability and accuracy of the solution can strongly depend on the chosen numerical schemes. Since the flow is dominated by convection for the given case only bounded schemes were used, namely the limited linear and upwind schemes. The OpenFOAM user guide states that these two schemes should give sufficient results and that higher order schemes are usually not necessary. A known problem of the upwind schemes is numerical diffusion caused by the fact that the value of any flow entity is constant over the whole cell as shown in Equation (3.28) [6]. The impact of this phenomenon is lower if the cell size is kept small and if the flow is aligned with the mesh, i.e. not diagonal. Higher order schemes could reduce this effect, but also lead to higher computational time. No investigations were

performed testing whether numerical diffusion occurred during the simulations but should be in future projects.

The simulation setup was the same as in Chapter 4.1 except for the schemes, which were switched to linear upwind for the velocity divergence terms and to upwind for the remaining divergence terms. The case was named `originalUpwind`.

As it turned out, the change from linear to upwind schemes did not have a big impact on the results but `originalUpwind` gave a filter pressure drop slightly closer to the given data. Thus, upwind schemes were used for the following simulations.

- **Turbulence model**

Three different turbulence models were tested during this project, namely the  $k$ - $\varepsilon$  model, the  $k$ - $\omega$ -SST model and the SPALART-ALLMARAS model. The former one was the industry standard for a long time for various applications, hence it was used as starting point for this project. However, the  $k$ - $\omega$ -SST model took over its place during the last years and is stated to give better results for highly complex geometries [6]. The motivation to use the SPALART-ALLMARAS model was an assumed saving of computational time. The simulation setups were similar to the ones before, i.e. medium cell size and upwind schemes. The cases were named `originalSST` and `originalSpAllm`.

The difference of the results and the computational time between  $k$ - $\omega$ -SST model and  $k$ - $\varepsilon$  model were rather small. Since the  $k$ - $\omega$ -SST model is commonly suggested, for example in [6] it was used for the following simulations.

### 4.2.2 Change of boundary conditions

For the cases described above the mass flow was equally divided between the two inlets. Since the operation pattern can change for the mist eliminator, three other distributions of mass flow were investigated. The first one was for 40% of the mass flow entering through the left inlet and 60% through the right one, the second one was with a ratio of 60%-40% and the last one with a ratio of 75%-25%. Since the flow was assumed to be incompressible this directly translated to changed velocities with the same ratios, namely 12.8 and 19.2 m/s, 19.2 and 12.8 m/s, and 24 and 8 m/s. All other properties were kept the same and the cases were named `originalVarU4060`, `originalVarU6040` and `originalVarU7525`.

### 4.2.3 Change of the geometry

The change of the geometry consisted of the modification of the inlet and outlet configuration and two cases were investigated. In both cases only two vertical outlet pipes with the diameter of the gathering pipe from the original case were used instead of three. For the first case with the name `topInletOutlet` the inlet pipes were attached vertically on top of the drum. For the second case called `topOutletMerged` the two outlet pipes were attached vertically and merged with a T-connection at a height of 1 m from the drum.

The motivation behind these changes was to compare different outlet header and inlet configurations and how the flow inside the drum would be affected by such arrangements. Especially, the second case was of interest due to the symmetrical setup which might give a more even flow distribution.

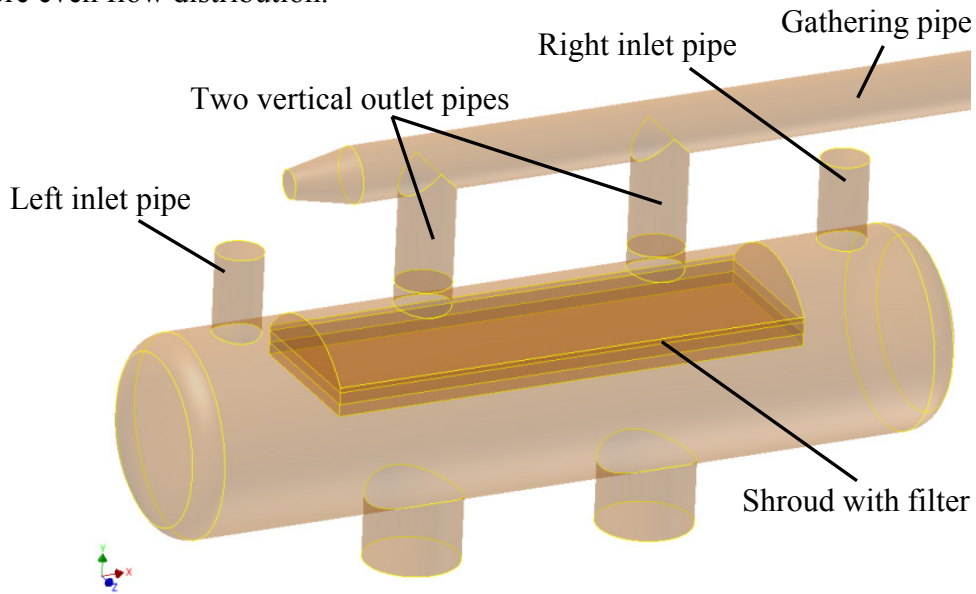


Figure 4.8: Eliminator design case *topInletOutlet*

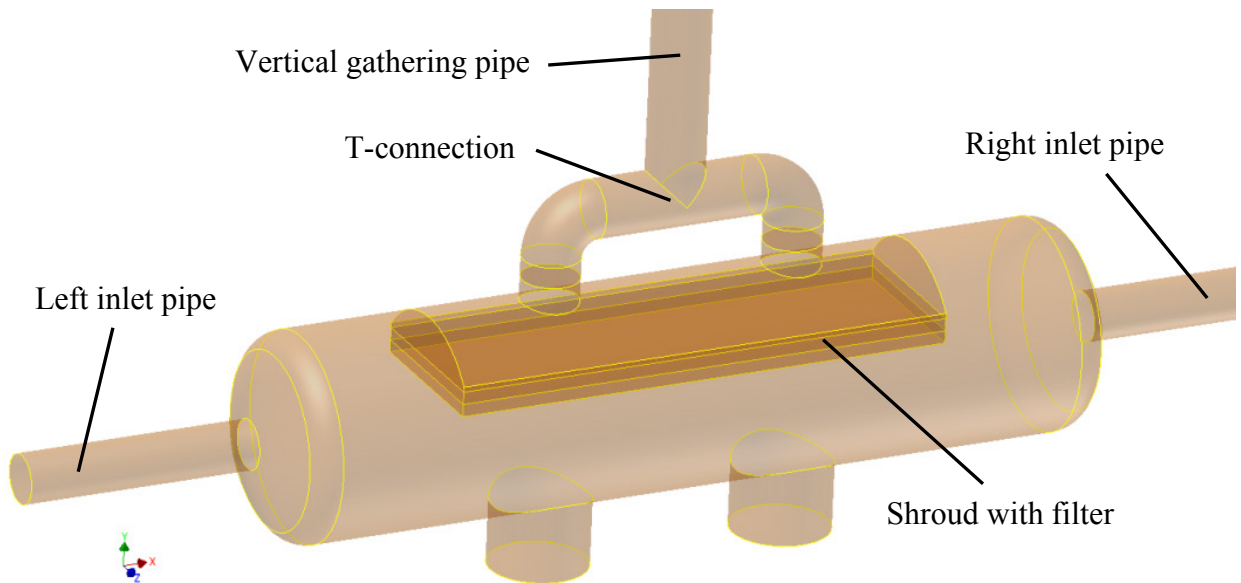


Figure 4.9: Eliminator design case *topOutletMerged*

The simulations with changed geometry were performed with the  $k-\omega$ -SST model, upwind schemes and a medium cell size.

An overview of all simulation variants is given in Table 4.5.

### 4.3 Evaluation criteria

Table 4.5: Overview of all simulation variants

Simulation name	Information	Number of cells	Numerical schemes	Turbulence model
originalCoarse	80 mm cell size	109,000	linear / limited linear	$k-\varepsilon$
originalRefined	filter and jet streams re-fined with 25 mm cells	945,000		
originalMedium	initial case, 50 mm cell size	449,000		
originalUpwind	changed numerical scheme			SPALART-ALLMARAS
originalSpAllm	variation of the turbulence model			
originalSST				
original4060	inlet vel. left: 12.8 m/s inlet vel. right: 19.2 m/s			
original6040	inlet vel. left: 19.2 m/s inlet vel. right: 12.8 m/s			
original7525	inlet vel. left: 24 m/s inlet vel. right: 8 m/s			
topInletOutlet	two vertical inlet and outlet pipes		upwind / linear upwind	$k-\omega$ -SST
topOutletMerged	two horizontal inlet pipes and two vertical outlet pipes merged into one			

### 4.3 Evaluation criteria

This chapter introduces the criteria and variables which were used to compare the simulations with each other. They include the velocity distribution in and the pressure drop over the filter, the total pressure drop over the whole eliminator, the volumetric flow distribution between the outlet pipes and their corresponding pressures. Further, visual evaluations by means of contour plots and computational criteria as the solver time were used.

### 4.3.1 Quantitative criteria

Important variables for the performance of the eliminator were used to compare the simulations with each other. These variables included the pressure drop over the filter, the overall pressure drop and the mass flow distribution for the outlet pipes. The filter pressure drop was also used for comparison with the manufacturer's data. The values for each variable were obtained by averaging over time after the fluctuations became rather small, i.e. less than 5% of the mean value. This was usually the case after 5 s.

- **Pressure drop over the filter**

Since the pressure drop over the filter is the only given data for validation, the values obtained from the simulations were used to estimate the quality of the simulations. To calculate the pressure drop in OpenFOAM the area weighted pressure values for the patches `porousIn` and `porousOut` were subtracted from each other.

- **Overall pressure drop**

The total pressure drop from the inlets to the outlet is an important criterion for future mist eliminator designs. Similar to the filter, the differences in average pressure between the patches `outlet` and `inletLeft` and `inletRight`, respectively, were calculated. The individual evaluation of each inlet offered an opportunity for better comparison between the simulations.

- **Pressure in the outlet header**

Another pressure value used for comparison was the average pressure in the outlet pipes. The faces intersecting the pipes perpendicularly were located 0.8 m above the patch `porousOut`, i.e. the filter outlet. The faces were named `pipeLeft`, `pipeMid` and `pipeRight`. Another face was used to observe the pressure in the gathering pipe located 1 m upstream of the outlet called `outletXSec`. The four patches are shown in Figure 4.10.

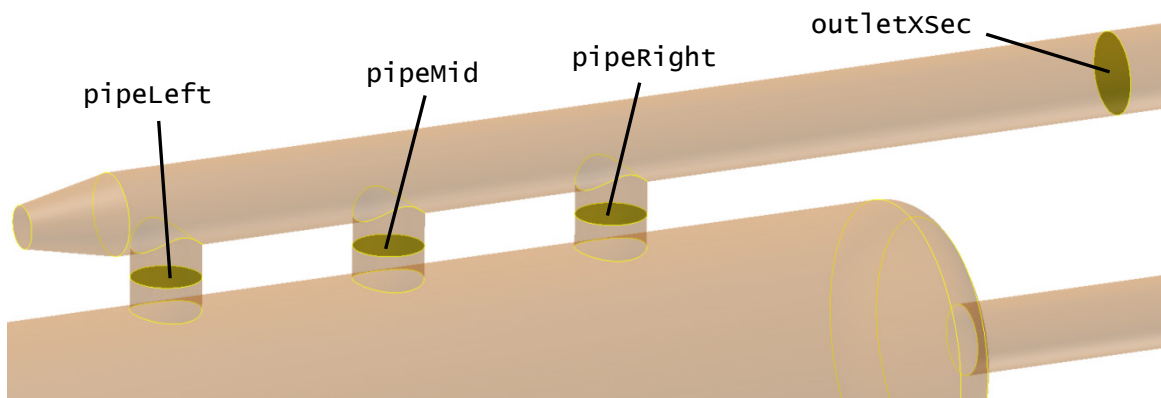


*Figure 4.10: The four patches used for data sampling*

- **Volumetric flow distribution between the vertical outlet pipes**

The flow distribution between the outlet pipes seemed to affect the flow pattern within the filter and was thus of interest. The same faces as for the pressure sampling described above were used.

### 4.3.2 Qualitative/visual criteria

Visual criteria include images and movies showing scalar or contour plots, vectors and streamlines. For the images, different faces were defined for plotting which are discussed in this chapter.

- **Cross sections through the CARTESIAN planes**

The origin of the coordinate system used to model the eliminator was located exactly in the center of the drum which made it practical to use the CARTESIAN planes. Especially the x-y plane was favorably used since it showed the development of the flow field inside the drum very well.

- **Cross section through the filter**

To evaluate, for example, the velocity distribution inside the filter a plane was created between the patches porousIn and porousOut. It was located exactly in the middle between the two mentioned planes.

### 4.3.3 Computational criteria

- **Computation time**

Particularly for future simulation projects which use the results obtained from this work, the computation time is an important evaluation parameter. It mainly depended on the cell size and the time step.

- **Convergence**

The simulation should run stably and reach convergence. For unsteady simulations the residuals cannot be used to check for convergence, but for example repetitive patterns in the flow distribution over the time steps could be an indicator. Also, the fluctuations of the quantitative values described in Chapter 4.3.1 may show such a behavior or could become stable at a certain value. If this is the case, it can be assumed that the solution is convergent. Large scale fluctuations in time may be falsely not considered if the simulated time is too short. For the cases described in this work, the simulation time was set to 10 s, which seemed to be sufficient. This was done after one case was run for 60 s and the averaged sampled values showed only minor fluctuations and the flow field seemed to be stabilized after 3 to 4 s already.

---

## 5 Results

The results obtained from the simulations described in the chapters above are discussed here in detail and possible conclusions are drawn. The initial case is evaluated and the first findings are discussed. Then, the simulation setup giving the most reasonable results is derived and the influence of a different velocity distribution for the inlets is evaluated. In a last step, the impact of geometry changes is described.

### 5.1 Initial case

The initial case originalMedium described in Chapter 4.1 could be run with good stability and convergence. The values already seemed to stabilize after two seconds of simulated time, i.e. no big fluctuations could be observed while visualizing the velocity plot over time. However, the simulation was run until 10 s were reached, to account for possible, larger, time dependent eddies. However, these could not be observed. The velocity plot of the xy-cross-section after 10 s is shown in Figure 5.1.

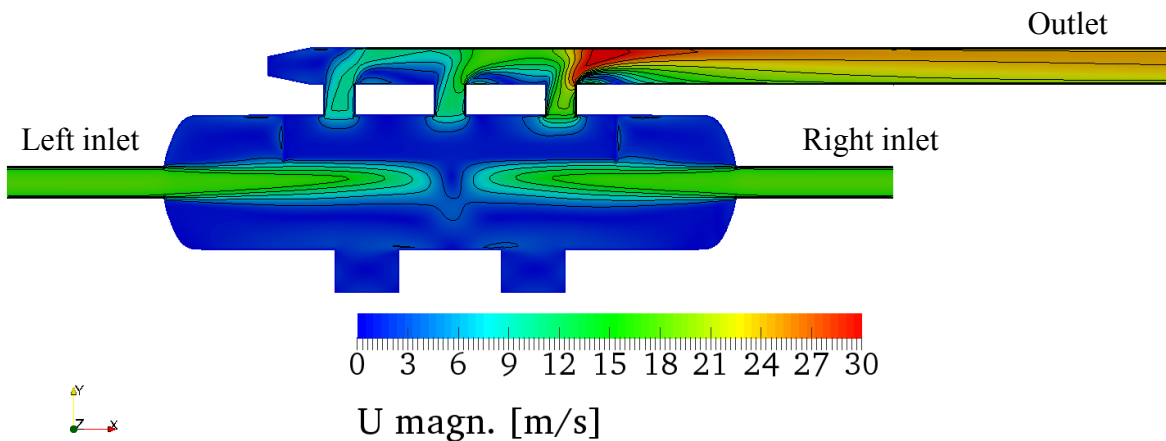


*Figure 5.1: Velocity distribution inside the mist eliminator for the initial case showing jet streams and separation in the outlet header*

As can be seen, the steam entered the drum as a jet stream due to its high inlet velocity, was slowed down in the filter and then accelerated in the vertical outlet pipes due to a decrease of the cross sectional area. The highest velocity could thus be found inside the horizontal gathering pipe at the outlet of the right vertical pipe.

What also could be observed was that the flow profile in the gathering outlet pipe is not fully developed and could have an impact on the flow field inside the drum. For the setup of future simulation projects the length of this pipe should thus be increased. To ensure comparability with the other simulations, the basic geometry was kept the same for this project.

## 5.1 Initial case

The pressure plot, shown in Figure 5.2, indicates that the main pressure losses occurred in the header due to strong separation caused by the sharp edges. This is especially the case for the right outlet pipe, where a large separation region established restraining the flow from the other outlet pipes. This is also illustrated in Figure 5.3 by the turbulent intensity, which is the ratio of the turbulent fluctuations  $U'$  over the mean flow velocity  $U$ . If the intensity is high, turbulence dominates the flow. From these results, one suggestion for an improved design could already be derived, i.e. to use bends in order to establish a smoother flow in the header.

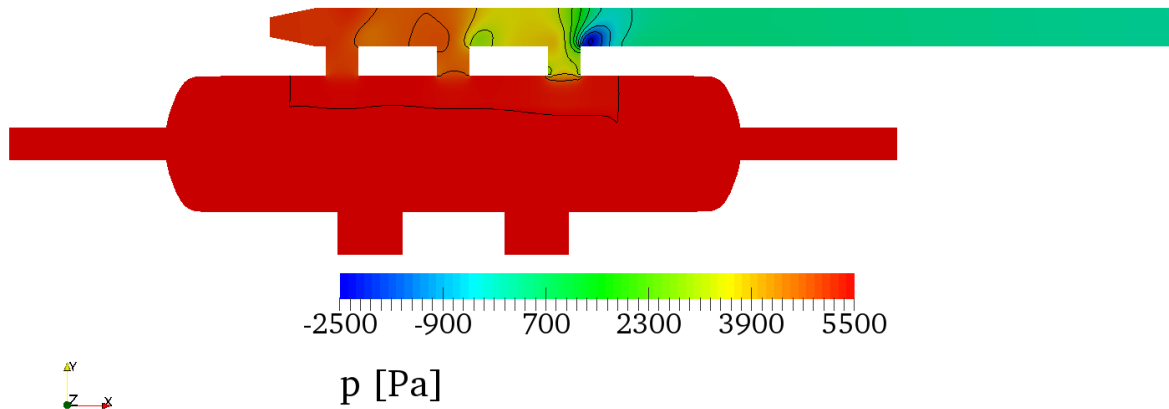


Figure 5.2: Pressure contour plot over the  $xy$ -plane inside the mist eliminator for the initial case showing the main pressure losses after the right outlet pipe

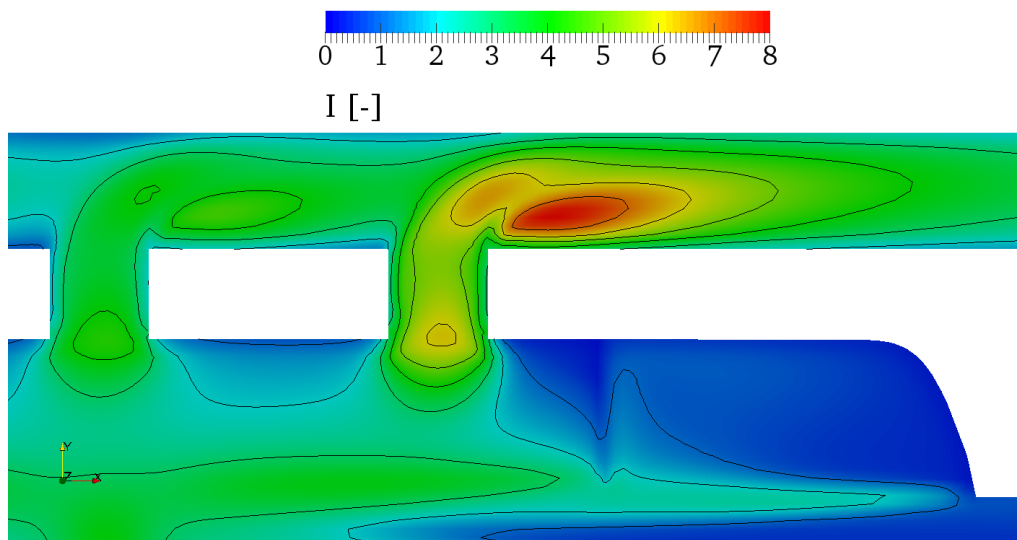
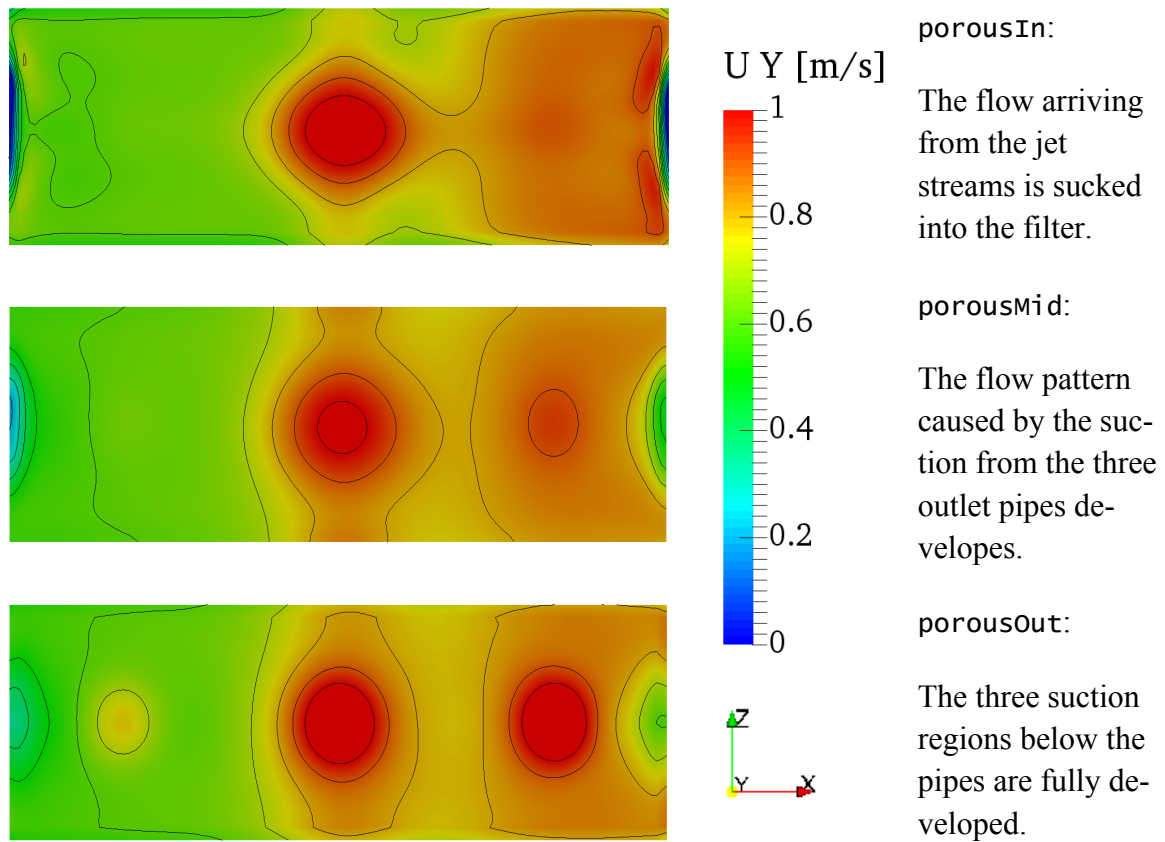


Figure 5.3: Turbulent intensity at the outlet pipes for the initial case showing turbulence in the mid and right outlet pipes and the gathering pipe

Another finding was that the flow distribution inside the filter was uneven and that strong suction below the outlet pipes caused the steam to travel faster through the filter in some regions. This effect is shown in Figure 5.4. As can be seen, the flow was mainly driven by



suction through the right and the middle pipe, even though the incoming flow was symmetrical. This indicates that the pressure gradients for these pipes are higher.



*Figure 5.4: Velocity components in y-direction filter inlet porousIn to filter outlet porousOut for the initial case showing the suction zones below the outlet pipes*

A good illustration of the flow distribution can also be provided by the stream line plot in Figure 5.5. It can be seen that the main share of steam flows through the right outlet pipe. Furthermore, the two eddies caused by the colliding jet streams and the resultant deceleration of the flow can be seen in the bottom part of the drum.

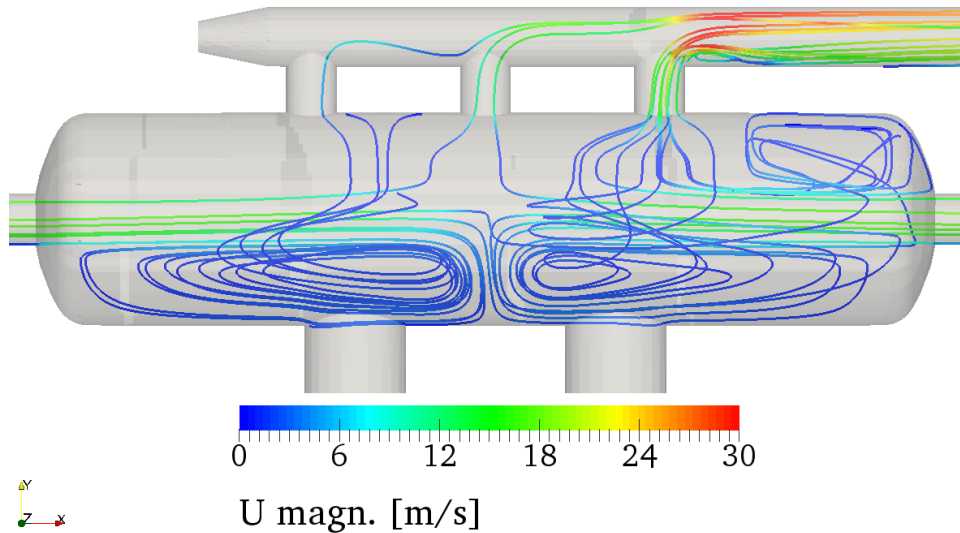


Figure 5.5: Velocity magnitude stream lines for the initial case showing that the main share of flow is sucked through the right outlet pipe

In Table 5.1, the mass flow distribution shows in numbers what could already be seen in the contour plots, namely that the main share of the flow travels through the middle and the right pipe. Further, the pressure drop over the filter seemed to fit the manufacturer's data well with a deviation of -2.9% which means that the method to implement the porous zone with the FORCHHEIMER coefficient seemed to be valid. Moreover, the pressure drop over the whole eliminator was around 5.6 kPa, independently from which inlet it was measured. Yet, the pressure difference for the right inlet was higher which could be the reason for the uneven flow distribution within the filter as was observed in Figure 5.4. With nine hours, this simulation had a moderate computation time.

Table 5.1: Results for the initial case after 10 s; values for the three outlet pipes from left to right are separated by a backslash (row 7 and 9)

	originalMedium
Turbulence model	$k-\varepsilon$
Number of cells	449,000
dp filter [Pa]	211.7
dp eliminator left [Pa]	5595
dp eliminator right [Pa]	5605
Pressure in outlet pipes from left to right [Pa]	4909 / 4567 / 3251
Pressure cross section outlet [Pa]	223.3
Mass flow distribution from left to right [%]	24.4 / 29.1 / 46.5
Simulation time [h]	9.1

A detailed description of the results obtained from the initial case was given in this chapter in order to point out general findings, which could be observed for all cases. In the following sections, only results which varied from the initial case are discussed.

## 5.2 Influence of the simulation setup

First, a mesh sensitivity analysis was performed based on the initial case. After an appropriate cell size could be found this case was used to evaluate different numerical schemes. When the decision was made for upwind schemes the turbulence model was changed and compared to the results obtained with the  $k-\varepsilon$  model for the upwind case. By choosing the  $k-\omega$ -SST model the last parameter for an appropriate simulation setup could be specified. With this setup the remaining simulations were run, namely the cases with variation of the inlet conditions and with changed geometry.

### 5.2.1 Mesh sensitivity

Three simulations with different cell sizes and numbers were performed in order to study how sensitive the results react towards a finer or coarser mesh. The other parameters were the same as for the initial case. The results are shown in Table 5.2 below.

*Table 5.2: Results for different mesh sizes*

	originalCoarse	originalMedium	originalRefined
Number of cells	109,000	449,000	945,000
Manufacturer's pressure drop [Pa]	215.3		
dp filter [Pa]	178.2	211.7	218.0
dp eliminator left [Pa]	5310	5595	5738
dp eliminator right [Pa]	5332	5605	5741
Pressure in outlet pipes from left to right [Pa]	4818 / 4485 / 3185	4909 / 4567 / 3251	4942 / 4600 / 3305
Pressure cross section outlet [Pa]	208.8	223.3	242.1
Mass flow distribution from left to right [%]	23.8 / 29.4 / 46.9	24.4 / 29.1 / 46.5	24.5 / 29.1 / 46.3
Simulation time [h]	2.0	9.1	17.8

As expected, the simulation with the finest mesh gave the best approach to the manufacturer's pressure drop of 215.3 Pa with a deviation of only 1.25%. However, the medium sized mesh was also very close to that value with only -2.98% deviation. In general, the differences between the refined and medium cases were rather small except for the pressure in the gathering pipe, which was 8% lower. Hence, it seemed reasonable to use a medium cell size for the remaining simulations, since the computational time was almost twice as high

## 5.2 Influence of the simulation setup

for the refined case, but the results did not show a big difference. The coarse mesh, however, should not be used, since it had a larger deviation of up to 18% compared to the refined case.

Another effect which could be observed was the increase of the pressure values for finer cell sizes as shown in Figure 5.6. An explanation for this behavior was the decrease in diffusion, due to a better resolution of the pressure gradients.

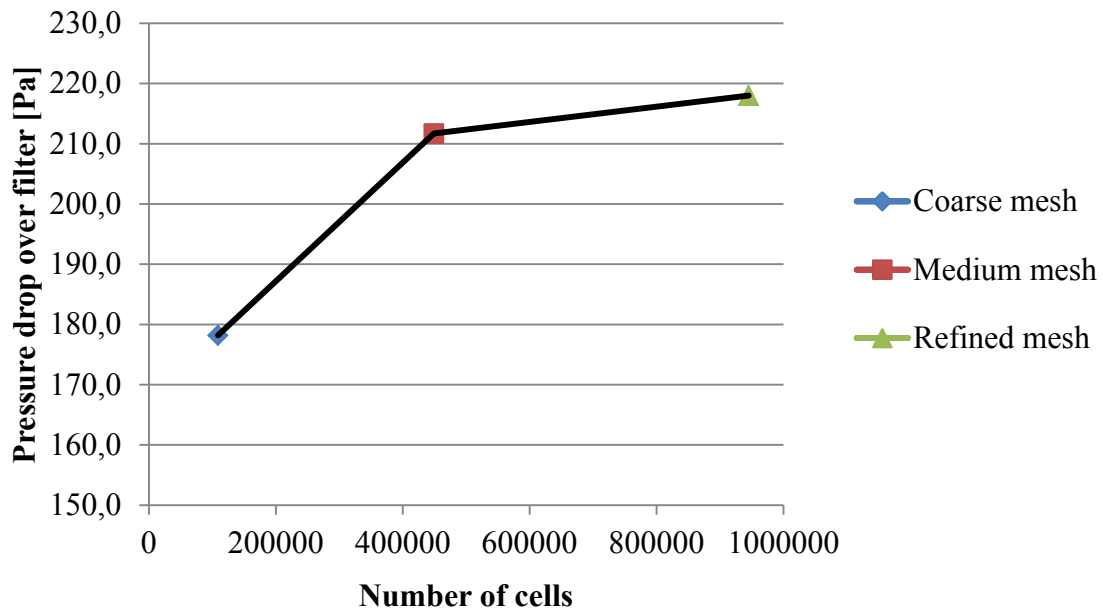


Figure 5.6: Pressure drop over the filter as function of the cell size

For further evaluations, the medium case was used as reference simulation, since cases with a refined mesh would have taken significantly more computational time and the difference between originalMedium and originalRefined was rather small.

### 5.2.2 Influence of the chosen numerical schemes

The numerical model was changed from limited linear to linear upwind. The remaining parameters were kept the same, i.e.  $k$ - $\epsilon$  turbulence modeling and a medium mesh size. The following results were obtained:

Table 5.3: Comparison of results between the initial case and the case run with upwind schemes

	originalMedium	originalUpwind
Numerical schemes	linear / limited linear	upwind / linear upwind
dp filter [Pa]	211.7	212.0
dp eliminator left [Pa]	5595	5523
dp eliminator right [Pa]	5605	5536
Pressure in outlet pipes from left to right [Pa]	4909 / 4567 / 3251	4848 / 4513 / 3321
Pressure cross section outlet [Pa]	223.3	215.3
Mass flow distribution from left to right [%]	24.4 / 29.1 / 46.5	24.7 / 29.6 / 45.6
Simulation time [h]	9.1	9.2

As can be seen most of the results were similar and the differences lay in between  $\pm 4\%$ . Also, the flow distribution seemed to be very similar, as for example the velocity distribution over the filter cross section showed, which is illustrated in Figure 5.7.

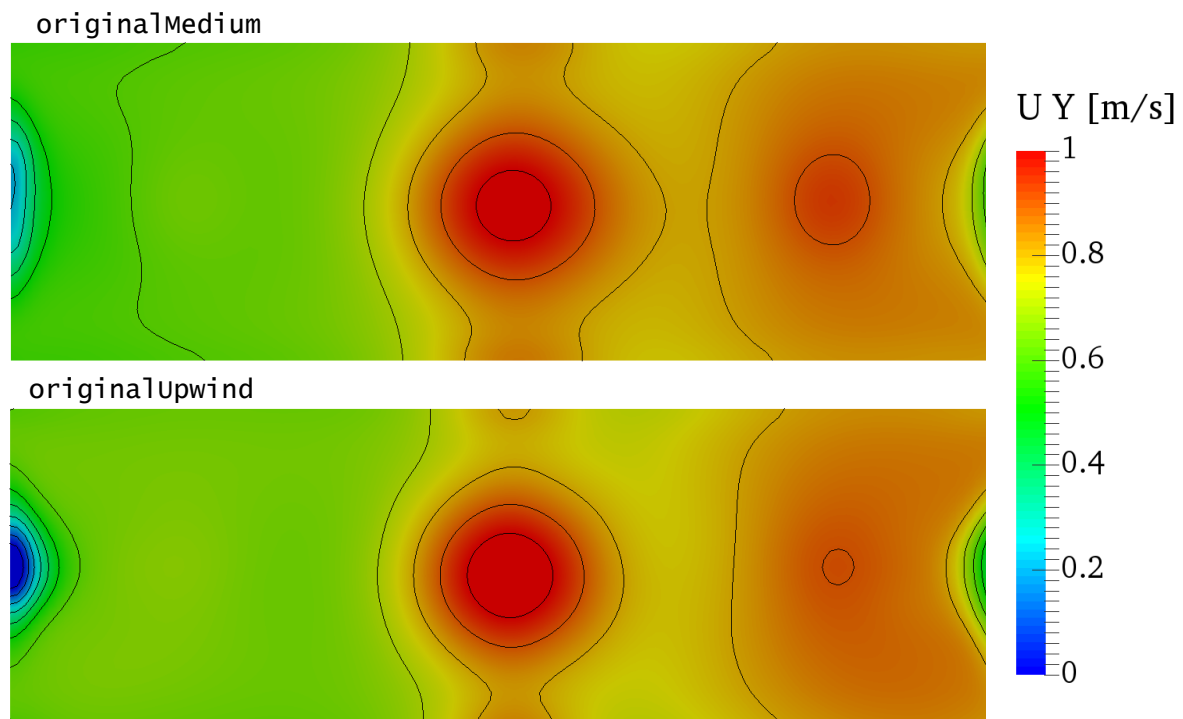


Figure 5.7: Comparison of the velocity distribution over the filter middle plane *porousMid* for the cases *originalMedium* and *originalUpwind*

Since the filter pressure drop was slightly closer to the data given by the manufacturer and the flow distribution showed a very similar behavior, upwind models were used for the following simulations and the case `originalupwind` was used as further reference.

### 5.2.3 Influence of the chosen turbulence models

Since the  $k-\varepsilon$  model is stated to be less accurate for simulations involving jet streams [6], which were present for the flow entering the drum, two additional turbulence models were tested, namely the  $k-\omega$ -SST and the SPALART-ALLMARAS model. The results are shown in Table 5.4 below.

*Table 5.4: Results for three different turbulence models for the initial design*

	<code>originalupwind</code>	<code>originalSST</code>	<code>originalSpAllm</code>
Turbulence model	$k-\varepsilon$	$k-\omega$ -SST	SPALART-ALLMARAS
dp filter [Pa]	212.0	210.3	208.9
dp eliminator left [Pa]	5523	5435	5364
dp eliminator right [Pa]	5536	5462	5379
Pressure in outlet pipes from left to right [Pa]	4848 / 4513 / 3321	4638 / 4266 / 3503	4484 / 4148 / 3153
Pressure cross section outlet [Pa]	215.3	202.9	202.2
Mass flow distribution from left to right [%]	24.7 / 29.6 / 45.6	26.6 / 32.0 / 41.3	26.5 / 31.1 / 42.3
Simulation time [h]	9.2	10.7	7.6

In general, Table 5.4 shows only minor differences between the applied turbulence models. A trend observed was that the pressure values were the highest for the  $k-\varepsilon$  and the lowest for the SPALART-ALLMARAS model. Further, the mass flow distribution between the vertical outlet pipes seemed to be more even for the case using the SST model with a range from 26.6% to 41.3% in contrast to the  $k-\varepsilon$  model with a range from 24.7% to 45.6%. This also applied for the range of the pressure distribution, which is the smallest for the SST model. One conclusion from that could be that the recirculation region caused by the flow separation at the right outlet pipe was smaller in the case of the SST model. This would be in accordance with the literature, stating that the  $k-\varepsilon$  model tends to over predict turbulence [15]. The contour plots below show such a behavior.

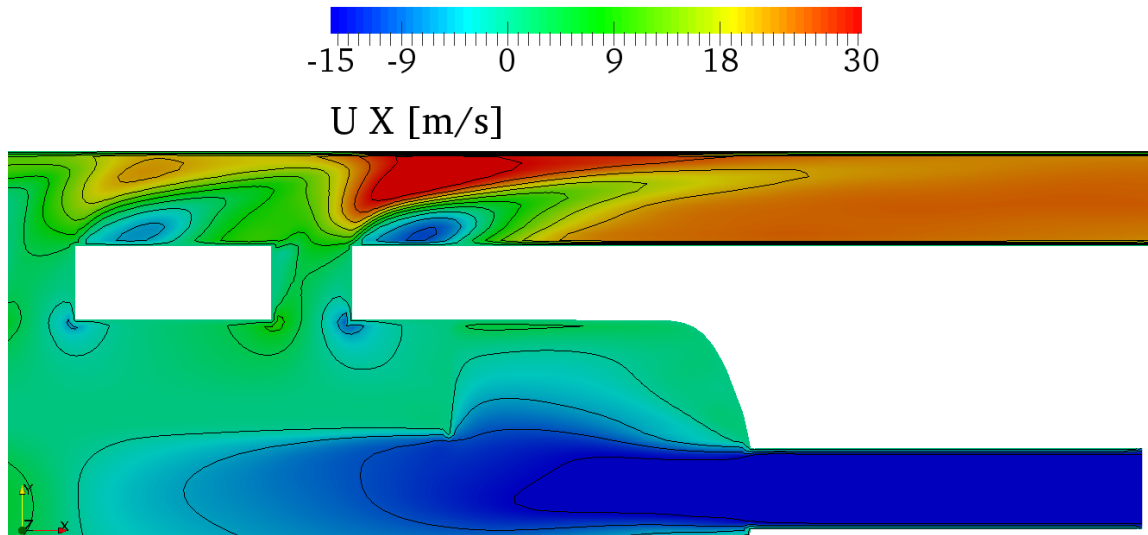


Figure 5.8: Velocity contour plot for the case *originalSST* showing the right upper corner of the *xy*-plane with gathering pipe and separation zones after the outlet pipes

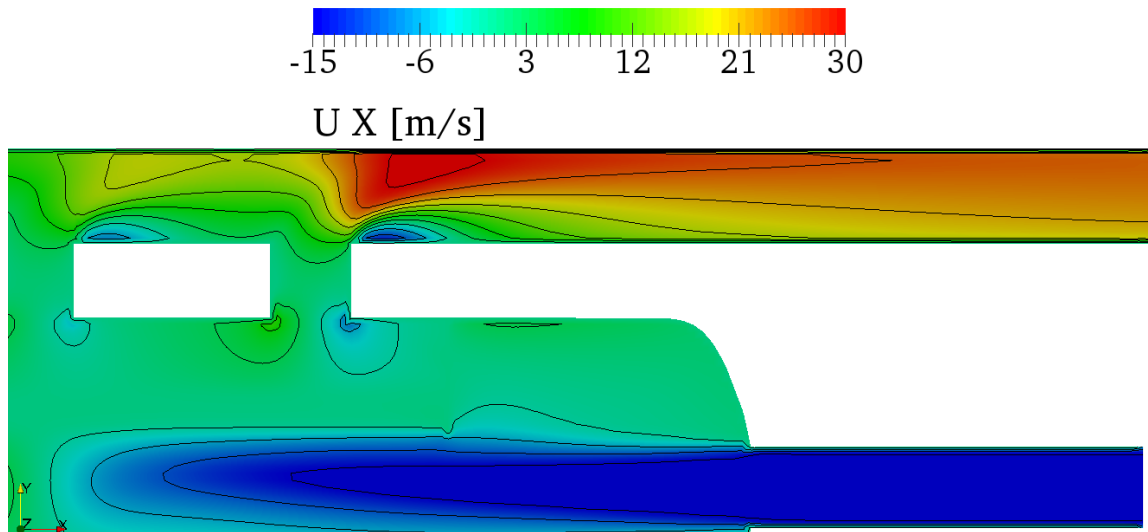


Figure 5.9: Velocity contour plot for the case *originalMedium* showing the right upper corner of the *xy*-plane with gathering pipe and separation zones after the outlet pipes

For the case using the  $k-\varepsilon$  model, the separation region in the gathering pipe reached much further downstream than for the SST model case as shown in Figure 5.8. This caused the flow to travel at higher velocities for a longer distance in the upper part of the pipe due to a lower cross sectional area and thus introduced a higher pressure drop caused by friction.

Further, the velocity profile in the filter cross section did not show major differences and was very similar to the ones in Figure 5.4.

The SPALART-ALLMARAS model as an example of a one-equation model gave an even lower pressure drop. The flow field seemed to be similar to the other two cases above as illustrated in Figure 5.10.

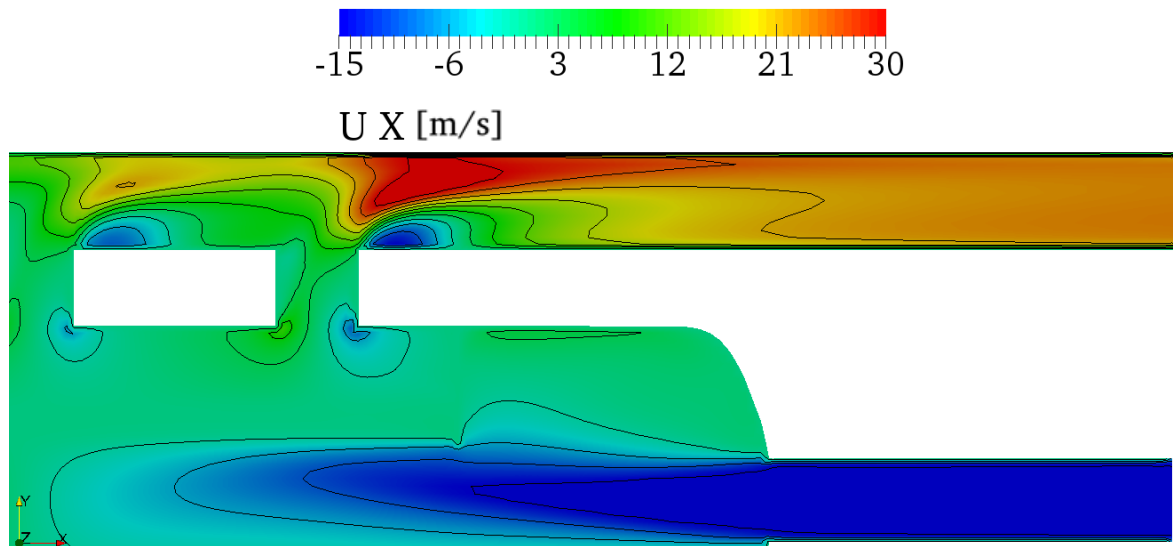


Figure 5.10: Velocity contour plot for the case *originalSpa11m* showing the right upper corner of the *xy*-plane with gathering pipe and separation zones after the outlet pipes

Unfortunately, the existence of only one parameter provided by the manufacturer made a validation very difficult and so was the choice for the right turbulence model. Since the evaluation variables showed not very big differences between each other and the visualization gave very similar flow patterns, it seemed that the solution was not very dependent on the turbulence model. Thus, the decision was made according to recommendations found in the literature. As already mentioned the  $k-\varepsilon$  model has problems estimating the extent of jet streams and separations and tends to over predict the resulting turbulence. On the other hand it uses wall functions, which do not require a high resolution of the boundary layer. This could be beneficial, since no  $y^+$ -adaptation was performed for the meshes used in this project. The SST model, however, requires very low  $y^+$ -values and could give wrong estimations for boundary layer flows. The strengths of the SST model rather lie in the modeling of separations and complex geometries in general. The SPALART-ALLMARAS model was originally developed for aerodynamic flows and is supposed to not be a suitable choice for internal flows and jet streams, yet it required less simulation time.

All in all, several sources (e.g. [6], [10]) state that the  $k-\omega$ -SST model is the state of the art turbulence model and should be applied for most cases in industry. Therefore, this model was chosen for the following simulations including the variation of the inlet conditions and the geometry changes.

## 5.3 Change of boundary conditions

After an appropriate simulation setup could be found including a medium cell size, upwind schemes and the  $k-\omega$ -SST model, the cases involving the variation of design parameters were run. First, the inflow distribution between the left and the right inlet was varied in the



ratios 40%-60%, 60%-40% and 75%-25% which led to the following inlet velocities: 12.8 / 19.2 m/s, 19.2 / 12.8 m/s and 24 / 8 m/s. The results are shown in Table 5.5 below.

*Table 5.5: Results of the inlet velocity variation for the initial design*

	original VarU4060	original SST	original VarU6040	original VarU7525
Inlet velocity left / right [m/s]	12.8 / 19.2	16 / 16	19.2 / 12.8	24 / 8
dp filter [Pa]	209.6	210.3	212.1	219.5
dp eliminator left [Pa]	5539	5435	5339	5155
dp eliminator right [Pa]	5413	5462	5494	5535
Pressure in outlet pipes from left to right [Pa]	4661 / 4641 / 3504	4638 / 4266 / 3503	4620 / 4241 / 3494	4592 / 4189 / 3454
Pressure cross section outlet [Pa]	202.6	202.9	203	202
Mass flow distribution from left to right [%]	27.0 / 31.7 / 41.3	26.6 / 32.0 / 41.3	26.1 / 32.4 / 41.5	25.3 / 32.7 / 42.0
Simulation time [h]	8.6	10.7	8.3	8.9

The pressure drop over the filter increased with higher velocities at the left inlet as illustrated in Figure 5.11. This led to the conclusion that the velocity within the filter also increased, since the pressure drop is directly proportional to it.

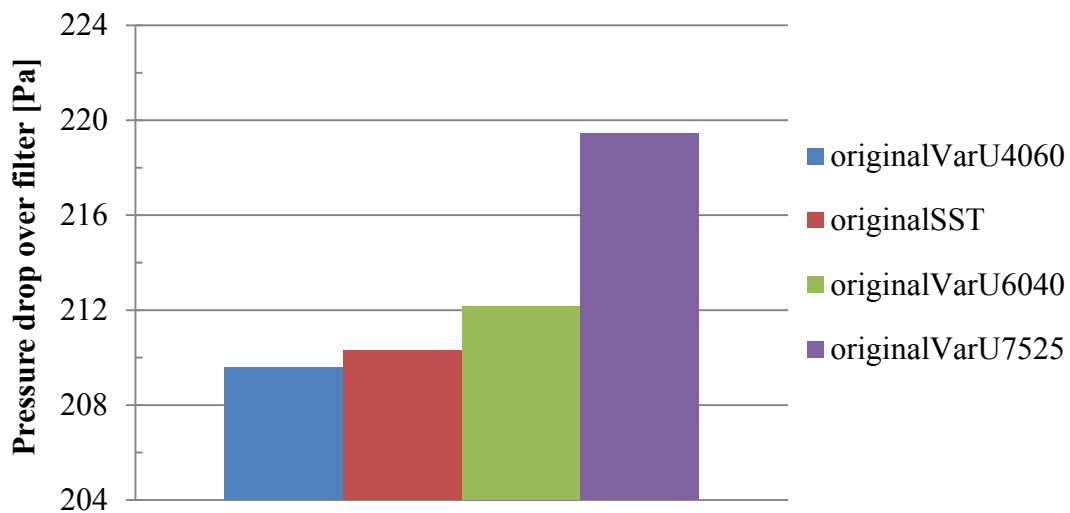


*Figure 5.11: Pressure drop over filter for different mass flow distributions at the inlets*

Further, the differences between the pressure losses calculated from the right and from the left inlet were higher with a less even distribution. The pressure drop for the side with a low inlet velocity was higher, which was not in accordance with the fact that the pressure losses are directly proportional to the velocity. However, the flow with a lower velocity

had to overcome the dynamic pressure caused by the high momentum of the fast flow during the collision and thus a higher static pressure for this side of the eliminator was necessary. Therefore, the inlet pressure for the low velocity side and consequently the pressure difference to the outlet was higher. This behavior is illustrated in Figure 5.12 showing the pressure distribution inside the eliminator drum for the case `originalVarU7525`. As can be seen the pressure is lower on the left side where the flow entered with a higher velocity.

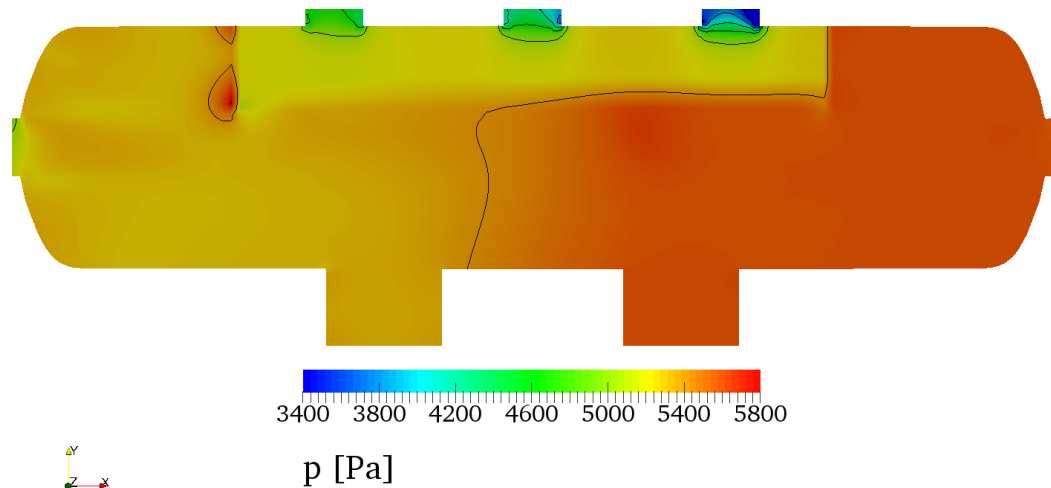


Figure 5.12: Pressure plot over the xy-plane inside the drum for the case `originalVarU7525` showing the pressure difference between the left and right part of the drum

Another effect observed was a different distribution of mass flow between the three outlet pipes. For the case `originalVarU4060` the range was the smallest with 14.3%. Thus, the flow was more evenly distributed causing lower velocities and hence a lower filter pressure drop. The different mass flow ranges for each case are shown in Figure 5.13.

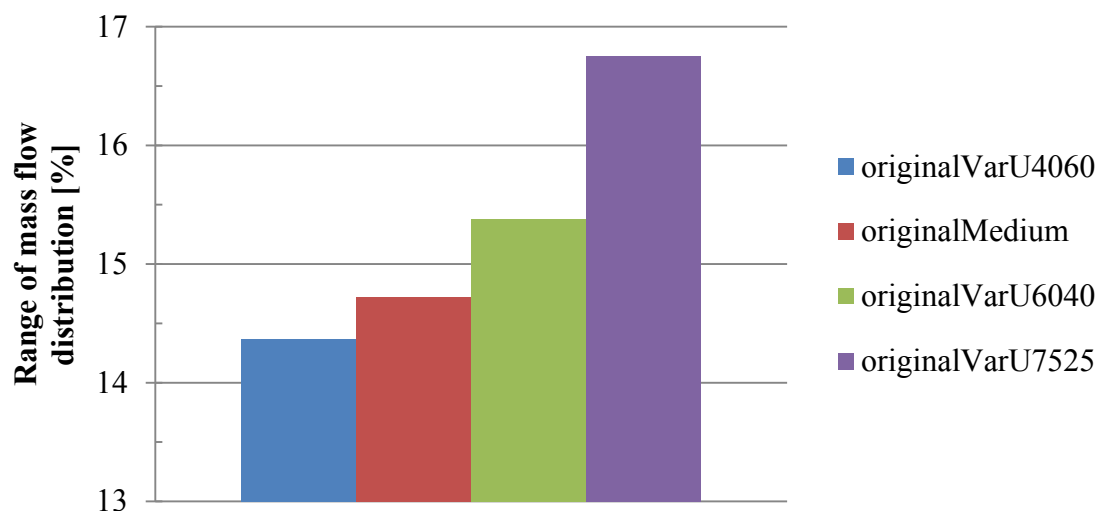


Figure 5.13: Mass flow ranges of the vertical outlet pipes for varying inlet velocities, e.g. for `originalVarU4060` 27% of the flow streamed through the left pipe and 41.3% through the right one, thus the mass flow range was 14.3%

This behavior could also be observed by the visualization of the flow field over the filter cross section `porousMid` as shown in Figure 5.14. There, the influence of the velocity variation and its impact on the suction zones within the filter can be seen. The higher the velocity at the left inlet the further right the main suction zone was located. Further, the gradient from the left to the right side of the filter seemed to be higher for the case `original-varU7525` and even a back flow into the drum due to underpressure caused by the left jet stream could be observed.

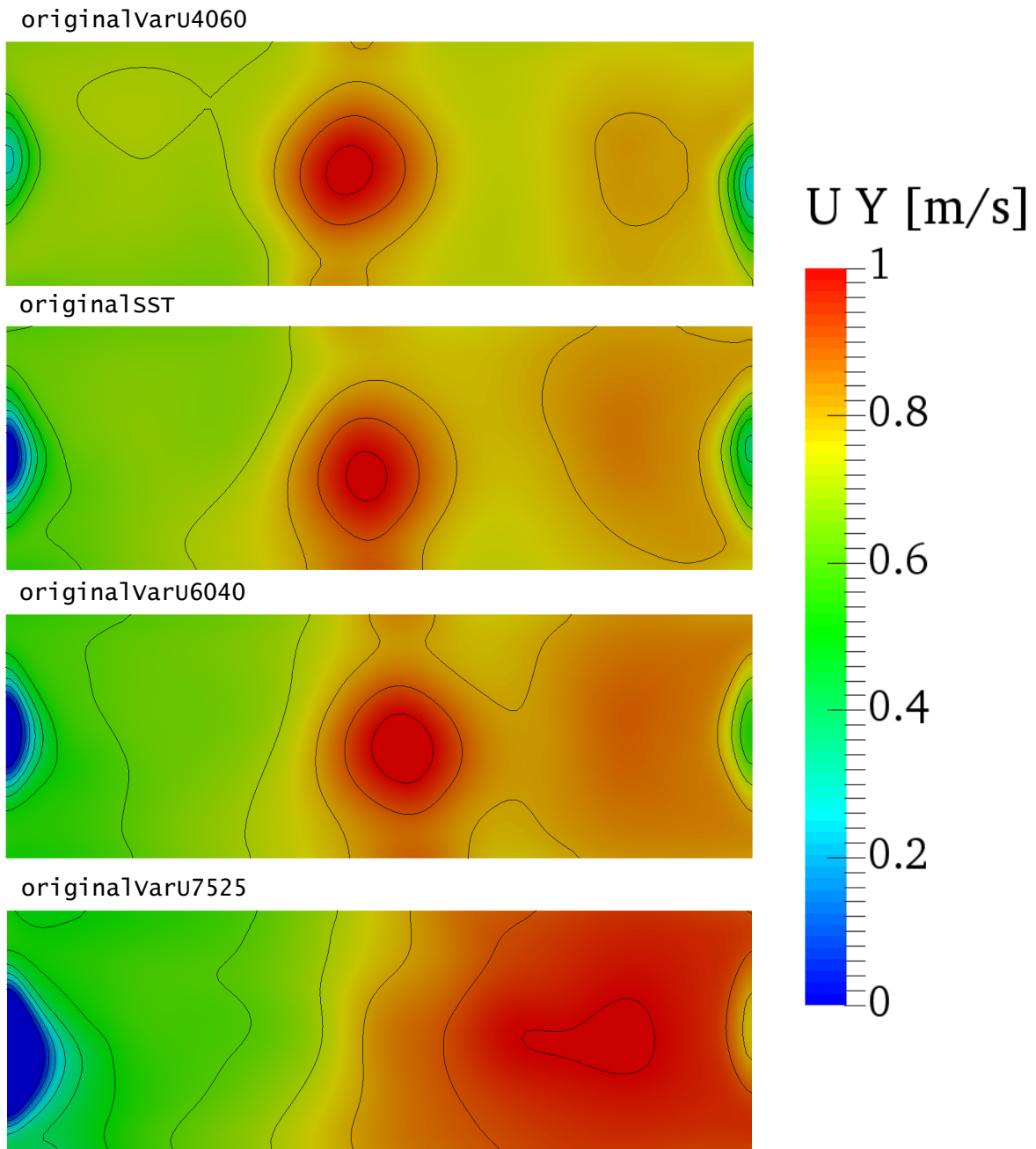
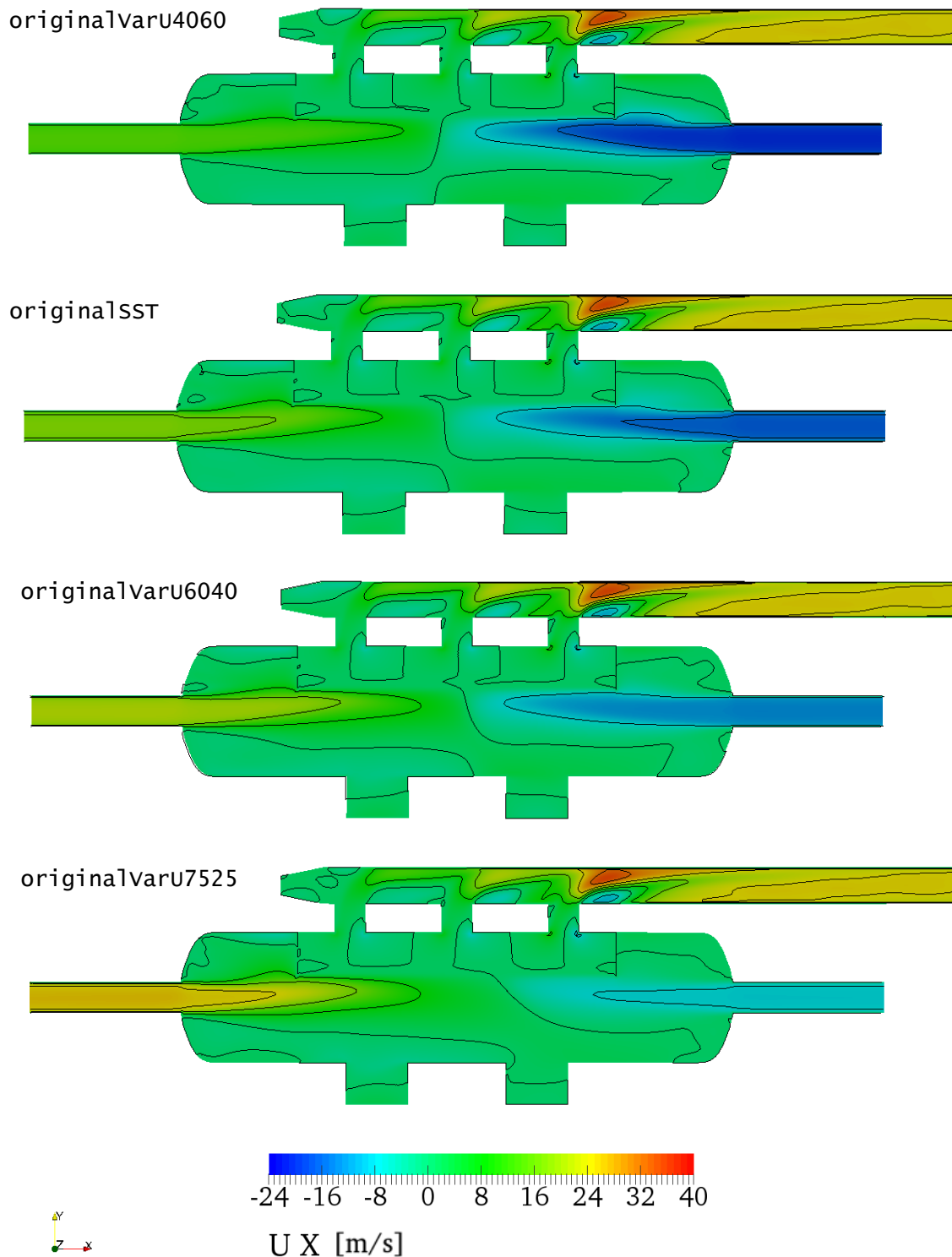


Figure 5.14: Velocity distribution over the filter middle plane `porousMid` for different inlet mass flows showing how the main suction zone moves further to the right with higher velocity at the left inlet

### 5.3 Change of boundary conditions

The velocity profiles over the xy-plane are illustrated in Figure 5.15. It shows the different velocities in the inlet pipes and how they affected the establishment of the jet streams. However, the impact in the outlet header was rather small.



*Figure 5.15: Velocity cross section over the xy-plane of the eliminator for different inlet velocities showing their impact on the development of the jet streams*

The simulations with varying inlet velocities showed that the pressure drop and velocity distribution could be manipulated by choosing different distributions of inlet mass flows. With lower velocities at the left inlet the pressure drop tended to decrease and the flow distribution within the filter seemed to be more even.

## 5.4 Geometry changes

Two additional eliminator designs were investigated, which are described in Chapter 4.2.3. The outlet and inlet configurations were changed in both cases to study the flow behavior for differently mounted mist eliminators. Other parameters were kept the same, i.e. the simulations were run with the medium sized mesh, upwind schemes and the  $k-\omega$ -SST turbulence model.

The results are shown below in Table 5.6.

*Table 5.6: Results for different outlet and inlet configurations*

	originalSST	topInletOutlet	topOutletMerged
Number of cells	449,000	482,000	436,000
dp filter [Pa]	210.3	201.2	209.3
dp eliminator left [Pa]	5435	5580	6550
dp eliminator right [Pa]	5462	5572	6551
Pressure in outlet pipes from left to right [Pa]	4638 / 4266 / 3503	4425 / 3574	5042 / 5073
Pressure cross section outlet [Pa]	202.9	130.0	107.6
Mass flow distribution from left to right [%]	26.6 / 32.1 / 41.3	42.7 / 57.3	50.3 / 49.7
Simulation time [h]	10.7	11.3	7.8

As can be noticed, the number of cells changed according to the volume of the model. Since for the case `topOutletMerged` the outlet header used the least space, the number of cells was the smallest. This was also the reason for the lower computation time. However, the size of the cells was not changed.

The pressure drops over the filter were similar to the reference case `originalSST` for the case `topOutletMerged`, however, the case `topInletOutlet` had a comparably lower one. This led to the conclusion that the velocities for this case were lower due to a higher deceleration inside the drum. This effect could be explained by the jet streams originating from the top and impinging the bottom wall which caused a higher loss in momentum and thus decreased the velocity. Furthermore, the jet streams were very unstable over time and showed a randomly oscillating behavior. This is illustrated in Figure 5.16 depicting the flow field inside the drum after two different periods of time.

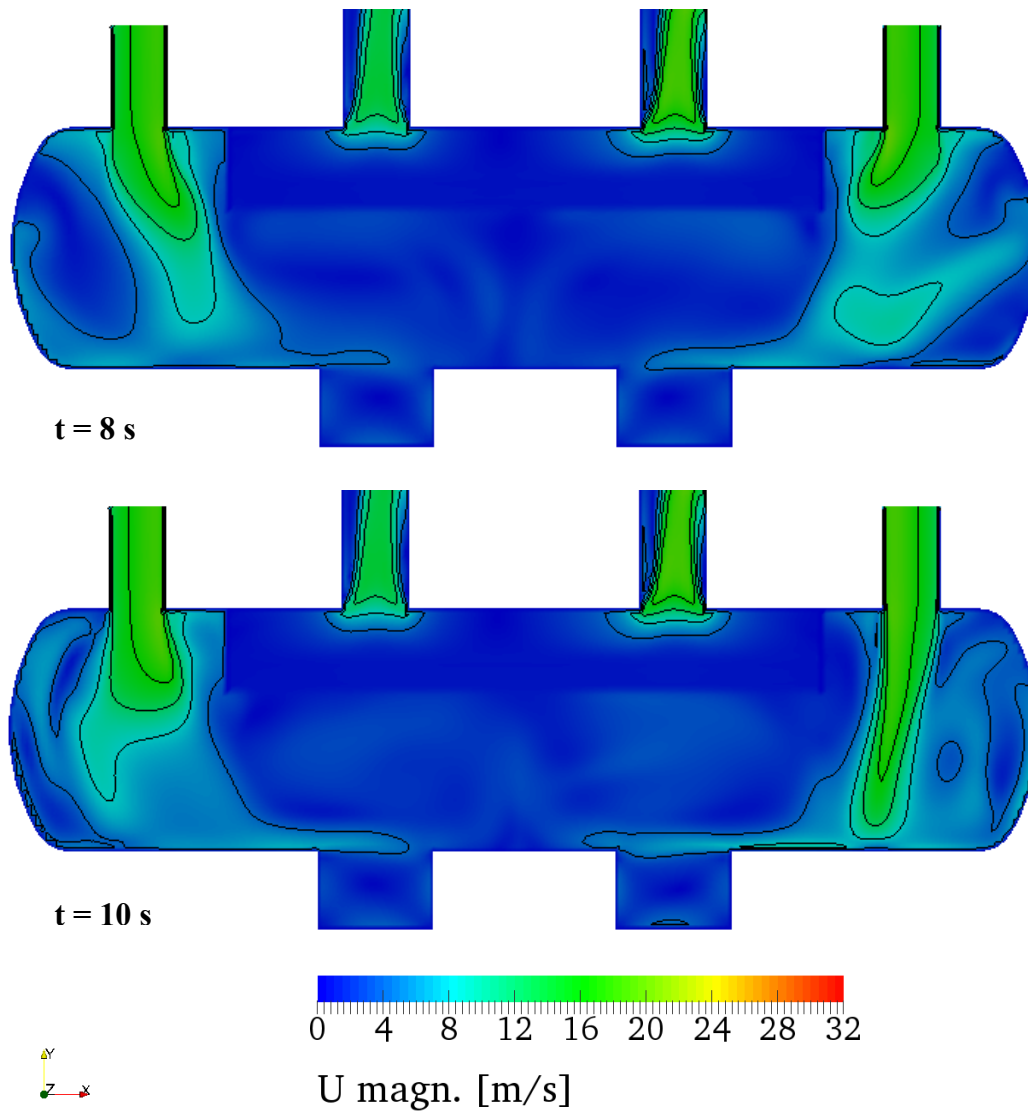


*Figure 5.16: Velocity contour plot over the  $xy$ -plane for the case `topInletOutlet` after two different periods of time showing the time dependency of the jet streams' shape*

By visualizing the velocity over the filter middle plane `porousMid` it could be observed that for the merged outlet case a symmetrical distribution was present after 10 s of simulated time. However, this state was not stable and the velocity fluctuated depending on the flow in the outlet pipe. This is shown in the two lower illustrations of Figure 5.17 depicting the flow distribution after two different periods of time.

A more even flow distribution was present for the case with the inlet pipes attached vertically from above. It seemed that the impingement with the bottom walls caused a greater loss of inertia than a collision of two jet streams.

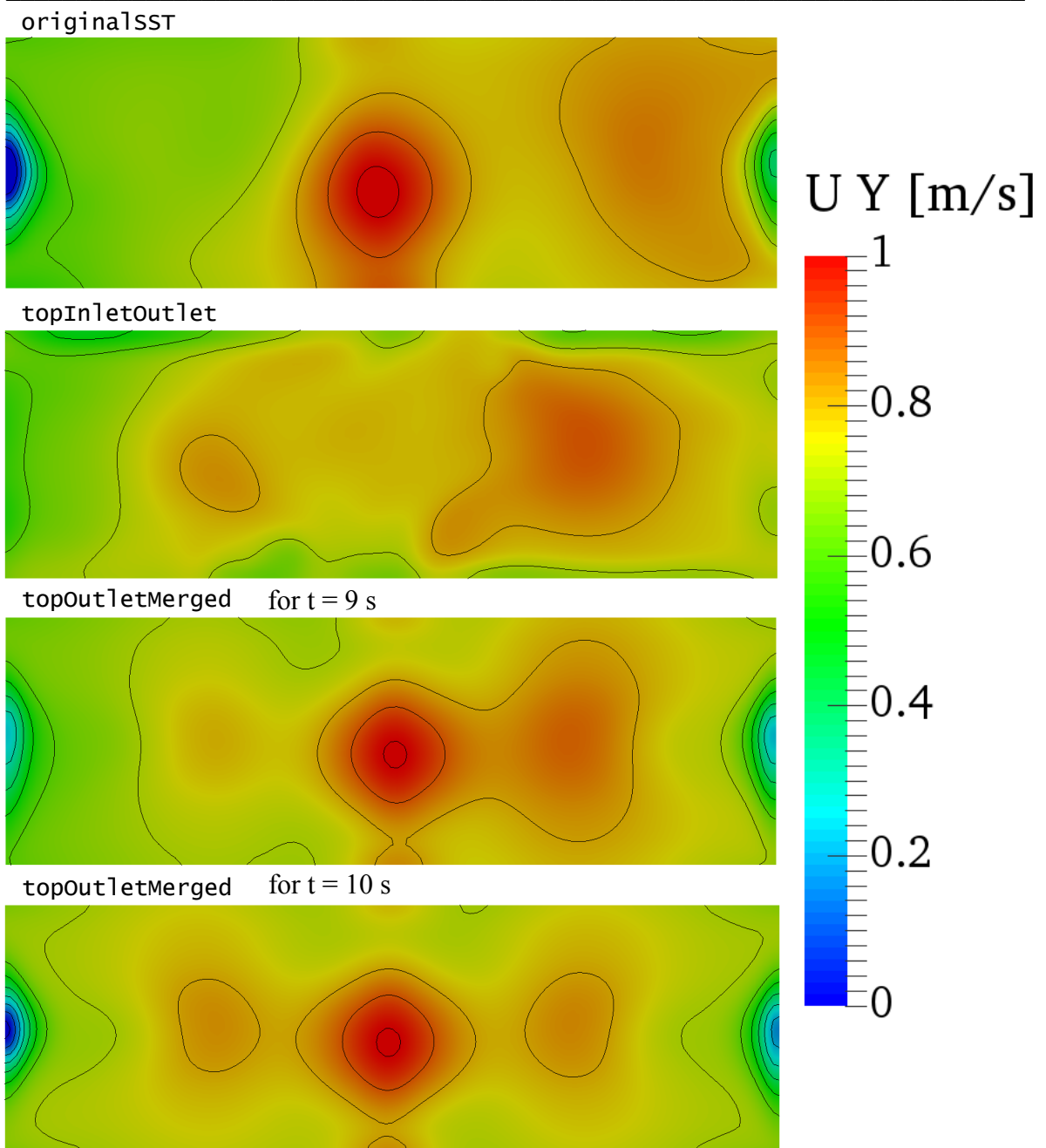


Figure 5.17: Velocity plot over the filter middle plane *porousMid* for different inlet and outlet configurations

As mentioned the flow lost more of its inertia due to the collision with the bottom wall. This behavior is illustrated in Figure 5.18 showing the turbulent intensity over the xy-plane. The turbulence in the center of the drum was low and as was observed in Figure 5.16, the main flow velocity was also small. Thus, the steam in the center of the drum could be assumed to be quite tranquilized in contrary to, for example, the case *topOutletMerged* where a more turbulent regime established.

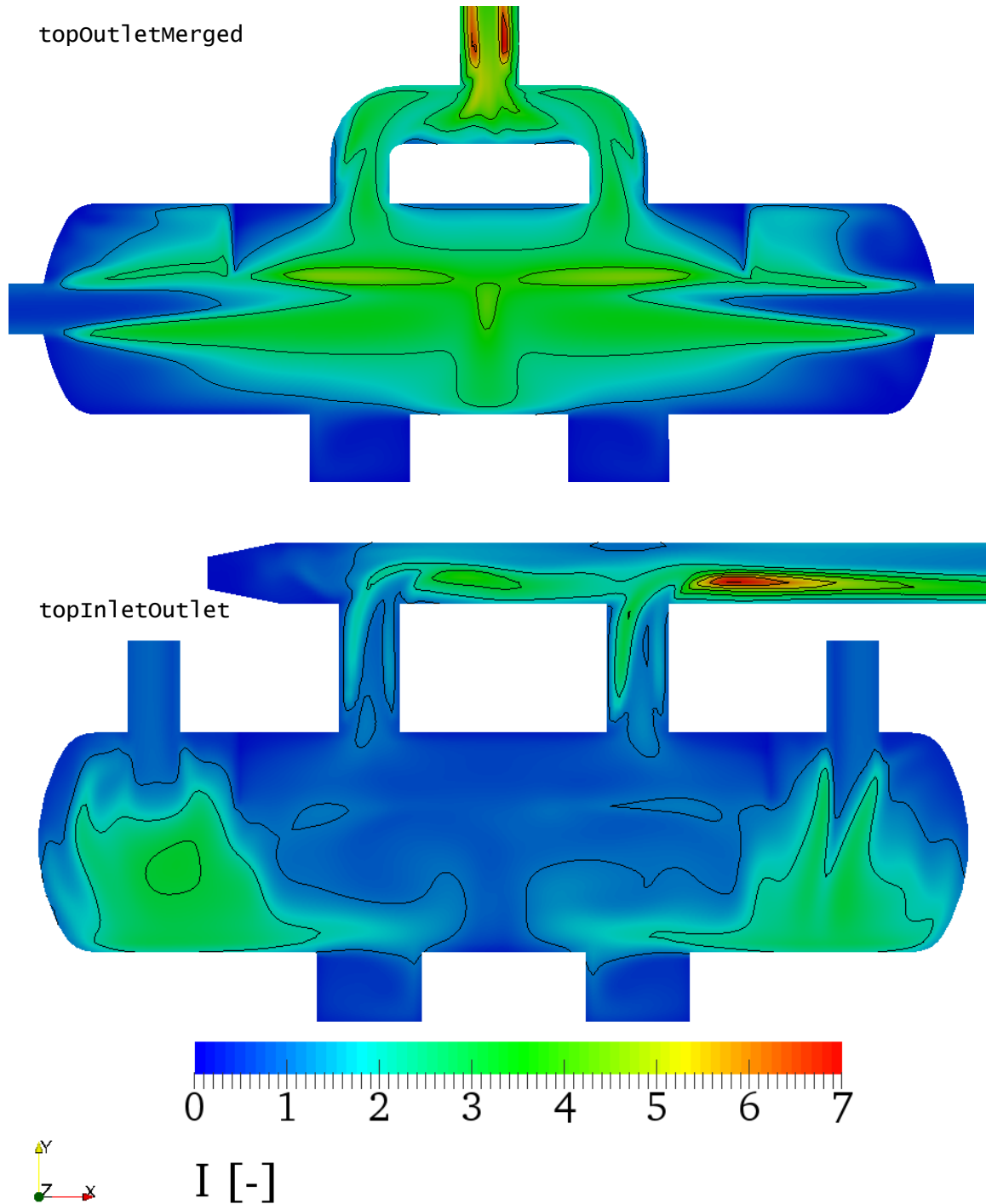


Figure 5.18: Turbulent intensity plot over the  $xy$ -plane for the case *outletMerged* and *topInletOutlet* showing a much more tranquilized regime for the latter case

The overall pressure drops increased for both cases but the case with the merged outlet had a 20% higher one. This was a significant difference compared to other pressure drops which deviated only around  $\pm 2\%$ . The reason for this could be found in the T-connection in the outlet header shown in Figure 5.19 and Figure 5.20. It can be observed, that there were strong regions of separation after the T-connection, causing a high pressure drop.



Also, the flow behavior was strongly time dependent as already mentioned above, which could be mostly observed further downstream in the outlet pipe.

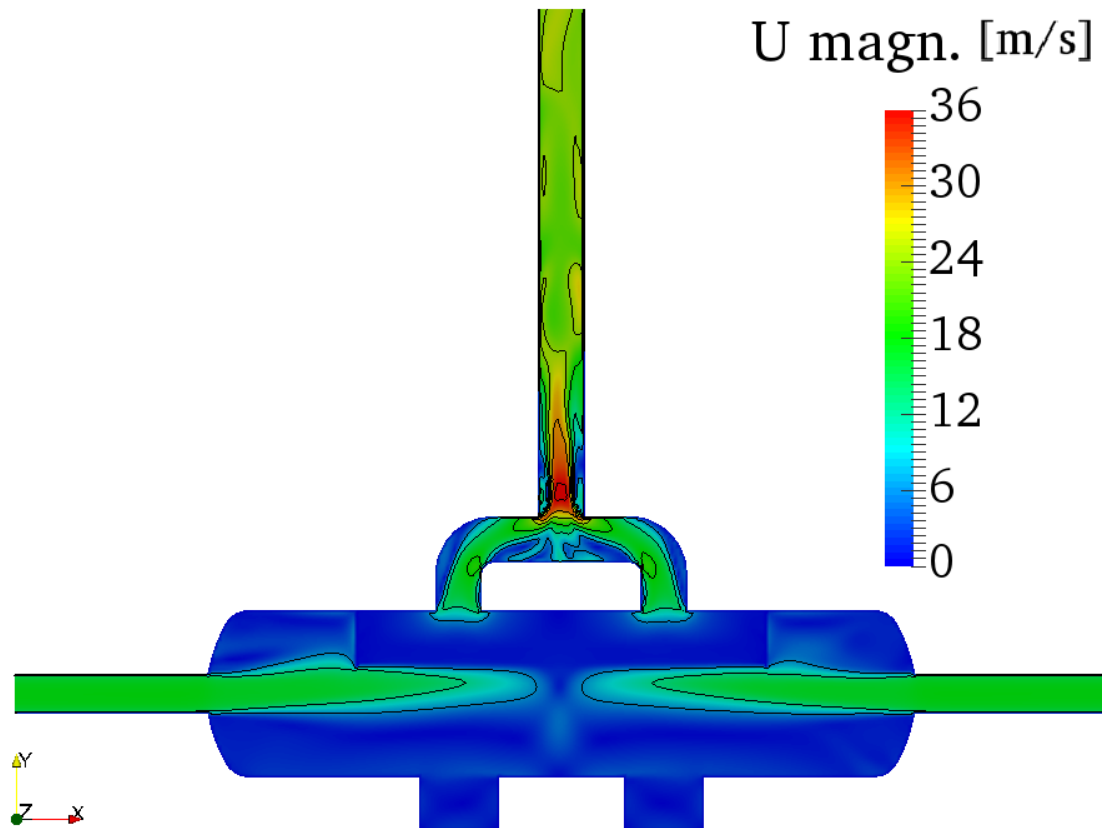


Figure 5.19: Velocity contour plot over the  $xy$ -plane for the case *topOutletMerged*

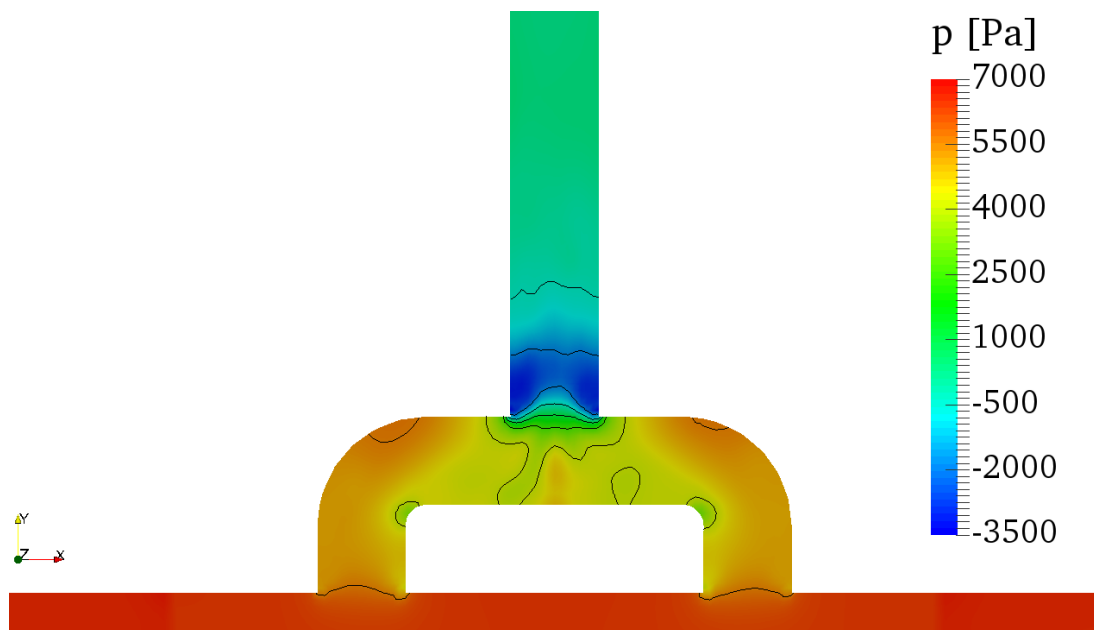


Figure 5.20: Pressure profile in the T-connection for the case *topOutletMerged* showing high pressure losses in the horizontal gathering pipe

Both simulated cases with changed geometry gave higher pressure drops than the initial design. The reduced number of outlet pipes caused higher velocities in them and thus increased the pressure loss. Furthermore, the sharp edges at connections of pipes led to strong separation. One recommendation would be to use steadier transitions, for example, bends or ducts. In general, the pressure drop can be kept small by using bigger pipe diameters and by avoiding abrupt transitions.

Further, a higher deceleration of the steam by the reduction of its inertia caused a better flow tranquilization in the center of the drum. Thus a more even flow distribution inside the filter was obtained, which could improve the separation efficiency.

## 5.5 Summary

In total, eleven simulations were performed during this project including three simulations as part of a mesh sensitivity analysis, one to investigate on different numerical schemes and two simulations with different turbulence models. Further, three simulations were run with changed inlet velocities and two used different inlet/outlet configurations. An overview of all simulation variants can be found in Table 4.5 and all results are listed in Appendix D.

As it turned out, a suitable simulation setup could be found by applying a mesh with a medium cell size of 50 mm, upwind schemes and the  $k-\omega$ -SST model. This setup was called `originalSST` and used as reference for the following simulations. However, the lack of sufficient measured data made the validation not very reliable. This needs to be considered if the results obtained from this work are used for any design decisions.

The contour plots showed that the current eliminator design utilizes the elimination of inertia by letting the two jet streams collide in the center of the drum. This caused turbulence and slowed down the flow. However, suction zones below the vertical outlet pipes established causing an uneven flow distribution inside the filter.

When the inlet velocities were varied according to their corresponding share of mass flow for the initial eliminator design, a better distribution of flow inside the filter could be found for higher velocities at the left inlet. In general, the pressure drops over the whole eliminator tended to be smaller for lower velocities. The most important results for the velocity variation are shown in Table 5.7.

Table 5.7: Summary of results obtained from varied inlet velocities

	original varU4060	original SST	original varU6040	original varU7525
Inlet velocity left / right [m/s]	12.8 / 19.2	16 / 16	19.2 / 12.8	24 / 8
dp filter [Pa]	209.6	210.3	212.1	219.5
Mass flow distribution from left to right [%]	27.0 / 31.7 / 41.3	26.6 / 32.0 / 41.3	26.1 / 32.4 / 41.5	25.3 / 32.7 / 42.0

Both newly developed designs with different outlet and inlet configurations caused higher pressure drops. The reason seemed to be the decrease of outlet pipes from three to two and the consequently increased velocities. Those caused more separation and thus greater pressure losses. An overview of the most important results obtained from the simulations with different eliminator geometries is given below in Table 5.8.

Table 5.8: Summary of results obtained from varied inlet/outlet configurations

	originalSST	topInletOutlet	topOutletMerged
dp filter [Pa]	210.3	201.2	209.3
Mass flow distribution from left to right [%]	26.6 / 32.1 / 41.3	42.7 / 57.3	50.3 / 49.7

A more even flow distribution could be obtained by the usage of vertically attached inlet pipes due to a better deceleration by collision with the bottom wall. This case seemed to be the most promising approach in terms of flow distribution within the filter and should be further investigated in future projects. With bends and ducts, this design could give a rather good performance.



---

## 6 Conclusion and outlook

A numerical analysis of the single-phase flow inside a horizontal mist eliminator was performed during this project using the free software OpenFOAM. Three major steps were realized throughout the work: the search for a suitable simulation setup, the variation of boundary conditions and the change of the simulated geometry. The first step consisted of three models with varying cell sizes, one with a different numerical scheme and two simulations with different turbulence models. The second step was accomplished by distributing the mass flow unevenly to the inlets and thus changing the inlet velocities. For the last step, two different inlet and outlet configurations were modeled where one model had inlet pipes attached vertically to the top of the drum and the other one had a vertical gathering pipe. The aim was to find an appropriate numerical setup in order to simulate the given problem and to investigate the influence of different design parameters on the performance of the eliminator.

The results obtained from the initial simulation case using the current eliminator design showed that applying the DARCY-FORCHHEIMER law yielded a close approach to the actual pressure drop over the filter supplied by the manufacturer. Furthermore, it could be observed that relatively high inlet velocities caused the establishment of jet streams, which eliminated their inertia by collision in the center of the drum. This slowed down the flow before it entered the filter and ensured a fairly even velocity distribution within the wire mesh. However, suction zones developed below the three vertical outlet pipes.

In the next step, the simulation parameters were changed. It turned out that a mesh with a medium cell size of 50 mm was sufficient and a refinement in regions of high velocity gradients did not give significant differences. The choice of a numerical scheme and a turbulence model was difficult due to the lack of appropriate measured data. Hence, the choice was based on recommendations found in the literature. All in all, a stable numerical model could be developed by using a medium sized mesh, upwind schemes, and the  $k-\omega$ -SST turbulence model.

The results showed that the variation of the inlet velocities could be used to manipulate the flow distribution inside the filter and thus the filter pressure drop. The higher the inflow rate from the right inlet, the more evenly distributed was the velocity. Further, higher pressure was necessary for the inlet with a low velocity, since the slower flow had to overcome the inertia of the faster one.

The two simulations with changed inlet and outlet configurations resulted in higher overall pressure losses in both cases. The reason for that was assumed to be the reduction of vertical outlet pipes from three to two and a consequently higher flow rate per pipe. This caused higher velocities and more separation, especially for the case with a vertical gathering pipe.

A good flow distribution was obtained from the case with vertical inlets. Due to better flow deceleration, the flow entered the filter from a more tranquilized regime.

For future projects, measurement data is essential in order to validate and verify the simulation setup. If higher computational power is available, the refined mesh and the incorporation of a  $y^+$ -adaptation should be employed to further ensure grid independency. Also, higher order numerical schemes could be applied. The validation of the turbulence model could be performed by a *Large Eddy Simulation* (LES). Further, the outlet pipes should be increased in length, to make the flow domain of interest independent from the outlet conditions. Also, investigations should be performed testing whether the assumption that the droplets are perfectly traveling with the flow is valid. This can be achieved by two-phase simulations.

Suggestions for improved designs would include bends and bigger pipe diameters to decrease the pressure drop. For a better flow distribution, vertical inlet pipes could be used. The financial effort for such design changes has to be compared to the savings achieved by such measures.

---

## References

- [1] Þ. Jóhannesson and G. Yngvi, "Mechanical Design of Geothermal Power Plants, Lecture 2, Drilling & Gathering Systems [lecture slides]," 2016 04 2016. [Online]. Available: <https://ugla.hi.is>.
- [2] M. H. Purnanto, S. J. Zarrouk and J. E. Cater, "CFD Modeling of Two-Phase Flow inside Geothermal Steam-Water," Star Energy Geothermal (Wayang Windu) Ltd., Indonesia, Auckland, New Zealand, 2012.
- [3] A. R. Pointon, T. D. Mills, G. J. Seil and Q. Zhang, "Computational Fluid Dynamic Techniques for Validating Geothermal Separator Sizing," Sinclair Knight Merz, Auckland, New Zealand, 2009.
- [4] N.A., "Cyclonic separation: Wikipedia," 14 April 2016. [Online]. Available: [https://en.wikipedia.org/wiki/Cyclonic\\_separation](https://en.wikipedia.org/wiki/Cyclonic_separation).
- [5] ACS Industries - Separation & Mass Transfer Products, "The Engineered Mist Eliminator," ACS Industries, Houston, Texas, 2004.
- [6] B. Andersson, R. Andersson, L. Håkansson, M. Mortensen, R. Sudiyo and B. van Wachem, Computational Fluid Dynamics for Engineers, Gothenburg: Cambridge University Press, 2015.
- [7] J. H. Ferziger and M. Perić, Numerische Strömungsmechanik, Berlin, Heidelberg: Springer, 2008.
- [8] J. E. Bardina, P. G. Huang and T. J. Coakley, "Turbulence Modeling Validation, Testing, and Development," Ames Research Center, Moffett Field, California, 1997.
- [9] Applied CCM Pty Ltd., "Caelus Documentation 4.10: 2.Theory," 2014. [Online]. Available: [http://www.caelus-cml.com/userdoc/2\\_Theory.html](http://www.caelus-cml.com/userdoc/2_Theory.html). [Accessed 19 April 2016].
- [10] C. Rumsey, "Turbulence Modeling Resource: NASA," 07 April 2016. [Online]. Available: <http://turbmodels.larc.nasa.gov/spalart.html>. [Accessed 21 April 2016].

- [11] C. J. Greenshields, OpenFOAM Programmer's Guide Version 3.0.1, N.A.: OpenFOAM Foundation Ltd., 2015.
- [12] H. Jasak, Error Analysis and Estimation for the Finite Volume Method with Applications to Fluid Flows, London: Imperial College, 1996.
- [13] H. E. Hafsteinsson, "Porous Media in OpenFOAM," Chalmers Technical University, Gothenburg, 2009.
- [14] C. J. Greenshields, OpenFOAM User Guide Version 3.0.1, N.A.: OpenFOAM Foundation Ltd., 2015.
- [15] N. G. Wright and G. J. Easorn, "Non-linear  $k-\epsilon$  turbulence model results for flow over a building at full-scale," *Applied Mathematical Modelling*, pp. 2010-1033, 4 September 2003.
- [16] O. Friedrich, Numerische Simulation und Analyse turbulenter Strömungen am Beispiel der Umströmung eines Zylinderstumpfes mit Endscheibe, Berlin: Universitätsverlag der TU Berlin, 2010.
- [17] E. D. Robertson, Verification, validation, and implementation of numerical methods and models for OpenFOAM 2.0 for incompressible flow, Mississippi: ProQuest LLC, 2015.
- [18] J. C. Puig, OpenFOAM Guide for Beginners, Barcelona: Universitat Politècnica de Catalunya, 2014.
- [19] R. DiPippo, Giethermal Power Plants, 2nd edition, Dartmouth, Massachusetts: Elsevier Ltd., 2008.



---

## Appendix A

*Estimation of the wall distance, i.e. the cell size of the first boundary layer for a  $y^+$ -value of 500 (maximum value stated in [6] for wall functions)*

The velocity of 30 m/s was obtained from simulations and was found in the outlet gathering pipe. The boundary layer height was assumed to be 0.2 m, which was almost the radius of the outlet pipe.

The REYNOLDS number in the boundary layer was:

$$Re_x = \frac{\rho UL}{\mu} = \frac{10.04 \frac{kg}{m^3} \cdot 30 \frac{m}{s} \cdot 0.2m}{1.6144 \cdot 10^{-5} \frac{kg}{m \cdot s}} = 37.4 \cdot 10^6 \quad (A.1)$$

The skin friction factor according to SCHLICHTING was:

$$C_f = (2 \log_{10}(Re_x) - 0.65)^{-2.3} = 0.0021 \quad (A.2)$$

The wall shear stress then became:

$$\tau_w = C_f \cdot \frac{1}{2} \rho U^2 = 0.0021 \cdot \frac{1}{2} \cdot 10.04 \frac{kg}{m^3} \cdot \left(30 \frac{m}{s}\right)^2 = 9.46 \frac{N}{m^2} \quad (A.3)$$

With which the friction velocity  $u_*$  could be calculated:

$$u_* = \sqrt{\frac{\tau_w}{\rho}} = \sqrt{\frac{9.46 \frac{N}{m^2}}{10.04 \frac{kg}{m^3}}} = 0.98 \frac{m}{s} \quad (A.4)$$

Finally, the wall distance became:

$$y = \frac{\mu y^+}{\rho u_*} = \frac{1.6144 \cdot 10^{-5} \frac{kg}{m \cdot s} \cdot 500}{10.04 \frac{kg}{m^3} \cdot 0.98 \frac{m}{s}} = 8.18 \cdot 10^{-5} m = 0.08 mm \quad (A.5)$$

---

## Appendix B

*Calculation of the turbulent boundary conditions, based on [6]*

The velocity at the inlet could be derived from the mass flow:

$$U_{in} = \frac{\frac{1}{2} \dot{m}_{tot}}{\frac{\pi}{4} D_{in}^2 \cdot \rho} = \frac{\frac{1}{2} 84 \frac{kg}{s}}{\frac{\pi}{4} (0.586 m)^2 \cdot 10.04 \frac{kg}{m^3}} = 15.51 \frac{m}{s} \approx 16 \frac{m}{s} \quad (B.1)$$

The REYNOLDS number in the inlet pipe was:

$$Re = \frac{U_{in} D_{in}}{\nu} = \frac{16 \frac{m}{s} \cdot 0.586 m}{1.61 \cdot 10^{-6} \frac{m^2}{s}} = 5.8 \cdot 10^6 \quad (B.2)$$

The turbulent intensity and length scale could then be calculated as follows:

$$I_T = 0.16 \cdot Re^{-\frac{1}{8}} = 0.16 \cdot (5.8 \cdot 10^6)^{-\frac{1}{8}} = 0.0228 \quad (B.3)$$

$$l_T = 0.07 \cdot D_{in} = 0.041 m \quad (B.4)$$

From that the turbulent kinetic energy, dissipation rate and viscosity could be estimated:

$$k_T = \frac{3}{2} \cdot (U_{in} \cdot I_T)^2 = 0.2 \frac{m^2}{s^2} \quad (B.5)$$

$$\varepsilon_T = C_\mu^{\frac{3}{4}} \cdot \frac{k_T^{\frac{3}{2}}}{l_T} = 0.359 \frac{m^2}{s^3} \quad (B.6)$$

$$\nu_T = \rho \cdot C_\mu \cdot \frac{k_T^2}{\varepsilon_T} = 0.1 \frac{m^2}{s} \quad (B.7)$$

For the simulations using the  $k-\omega$  model also the specific dissipation had to be specified:

$$\omega_T = \frac{\varepsilon_T}{(k_T \cdot 0.19)} = 9.43 s^{-1} \quad (B.8)$$

---

## Appendix C

### *Calculation of the FORCHHEIMER coefficient*

The velocity in the filter could be obtained from the volumetric flow:

$$Q = 2 \frac{U_{in} \pi}{4 D_{in}^2} = 2 \frac{16 \frac{m}{s} \cdot \pi}{4 \cdot (0.586 \text{ m})^2} = 8.36 \frac{m^3}{s} \quad (C.1)$$

Thus, the velocity in the filter was:

$$U_f = \frac{Q}{l_f w_f} = \frac{8.36 \frac{m^3}{s}}{5.976 \text{ m} \cdot 1.915 \text{ m}} = 0.73 \frac{m}{s} \quad (C.2)$$

The FORCHHEIMER coefficient could now be obtained by rearranging Equation (3.35) and neglecting the DARCY coefficient:

$$f = \frac{2 dp}{\rho U_f dx_f} = \frac{2 \cdot 215.3 \text{ Pa}}{10.04 \frac{kg}{m^3} \cdot 0.73 \frac{m}{s} \cdot 0.3 \text{ m}} = 251.3 \quad (C.3)$$

# Appendix D

Overview of all simulation results; the rows in bolt are used as reference for the simulations in the following section below

Simulation	deltaPFilter [Pa]	difference [%]	deltaPElimi natorLeft [Pa]	difference [%]	deltaPElimi natorRight [Pa]	difference [%]	pressure PipeLeft [Pa]	difference [%]	pressure PipeMid [Pa]	difference [%]
manufacturer's data	215,3		3700		3700					
<b>originalMedium</b>	<b>211,7</b>	<b>-1,67</b>	<b>5595</b>	<b>51,22</b>	<b>5605</b>	<b>51,49</b>	<b>4909</b>		<b>4567</b>	
originalRefined	218,0	1,25	5738	55,08	5741	55,16	4942		4600	
originalCoarse	178,2	-17,23	5310	43,51	5332	44,11	4818		4485	
<b>originalUpwind</b>	<b>212,0</b>	<b>0,14</b>	<b>5523</b>	<b>-1,29</b>	<b>5536</b>	<b>-1,23</b>	<b>4848</b>	<b>-1,24</b>	<b>4513</b>	<b>-1,18</b>
<b>originalSST</b>	<b>210,3</b>	<b>-0,80</b>	<b>5435</b>	<b>-1,59</b>	<b>5462</b>	<b>-1,34</b>	<b>4638</b>	<b>-4,33</b>	<b>4266</b>	<b>-5,47</b>
originalSpAll	208,9	-1,46	5364	-2,88	5379	-2,84	4484	-7,51	4148	-8,09
originalVarU4060	209,6	-0,33	5539	1,91	5413	-0,90	4661	0,50	4641	8,79
originalVarU6040	212,1	0,88	5339	-1,77	5494	0,59	4620	-0,39	4241	-0,59
originalVarU7525	219,5	4,35	5155	-5,15	5535	1,34	4592	-0,99	4189	-1,80
topInletOutlet	201,2	-4,33	5580	2,67	5572	2,01	4425	-4,59		-100,00
topOutletMerged	209,3	-0,48	6550	20,52	6551	19,94	5042	8,71		-100,00

Simulation	pressurePipe Right [Pa]	difference [%]	pressureOut letXSec [Pa]	difference [%]	fluxPipeLeft [m³/s]	difference [%]	fluxPipe Mid [m³/s]	difference [%]	fluxPipe Right [m³/s]	difference [%]
manufacturer's data										
<b>originalMedium</b>	<b>3251</b>		<b>223,3</b>		<b>2,07</b>		<b>2,47</b>		<b>3,95</b>	
originalRefined	3305		242,1		2,08		2,47		3,93	
originalCoarse	3185		208,8		1,99		2,46		3,93	
<b>originalUpwind</b>	<b>3321</b>	<b>2,15</b>	<b>215,3</b>	<b>-3,58</b>	<b>2,10</b>	<b>1,40</b>	<b>2,51</b>	<b>1,78</b>	<b>3,87</b>	<b>-1,95</b>
<b>originalSST</b>	<b>3503</b>	<b>5,48</b>	<b>202,9</b>	<b>-5,76</b>	<b>2,26</b>	<b>7,67</b>	<b>2,72</b>	<b>8,19</b>	<b>3,51</b>	<b>-9,37</b>
originalSpAll	3153	-5,06	202,2	-6,08	2,25	7,19	2,64	5,01	3,59	-7,30
originalVarU4060	3504	0,03	202,6	-0,15	2,29	1,33	2,69	-1,10	3,51	0,00
originalVarU6040	3494	-0,26	203	0,02	2,22	-1,99	2,75	1,10	3,52	0,28
originalVarU7525	3454	-1,40	202	-0,23	2,14	-5,18	2,78	2,05	3,56	1,55
topInletOutlet	3574	2,03	130	-35,93	3,63	60,62		-100,00	4,87	38,75
topOutletMerged	5073	44,82	107,6	-46,97	4,27	88,94		-100,00	4,22	20,23